NOVA SCHOOL OF
SCIENCE & TECHNOLOGY

DEPARTMENT OF MATERIALS SCIENCE

GUILHERME DINIS DIAS VALENTE

BSc in Materials Science and Engineering

DESIGNING SURFACTANT IONIC LIQUID-BASED COMPOSITES FOR CO_2 CAPTURE AND CONVERSION

INTEGRATED MASTER IN MATERIALS ENGINEERING

NOVA University Lisbon

OCTOBER, 2024

DEPARTAMENT OF MATERIALS SCIENCE

DESIGNING SURFACTANT IONIC LIQUID-BASED COMPOSITES FOR CO_2 CAPTURE AND CONVERSION

GUILHERME DINIS DIAS VALENTE

BSc in Materials Science and Engineering

Adviser: Doctor Marta Corvo
Principal Researcher, i3N|CENIMAT, NOVA School of Science and Technology

Co-advisers: Doctor Raquel Barrulas
Researcher, Faculty of Science and Technology, University of Twente

Examination Committee:

Chair: Doctor Maria Helena Figueiredo Godinho
Associate Professor, NOVA School of Science and Technology

Rapporteurs: Doctor Marcileia Zanatta
Researcher at the Institute of Advanced Materials, Universitat Jaume I

Adviser: Doctor Marta Corvo
Principal Researcher, i3N|CENIMAT, NOVA School of Science and Technology

INTEGRATED MASTER IN MATERIALS ENGINEERING

NOVA University Lisbon
October, 2024

Designing Surfactant Ionic Liquid-Based Composites for CO_2 Capture and Conversion

À minha mãe Dulce e ao meu pai Carlos.

ACKNOWLEDGMENTS

Gostaria de prestar o meu maior agradecimento à minha orientadora Professora Marta Corvo e co-orientadora Dra. Raquel Barrulas, por todo o conhecimento que me passaram e apoio demonstrado durante os últimos 9 meses. Quero agradecer especialmente aos meus colegas de laboratório Rodrigo, Clarisse e Emanuel por todos os momentos, partilhas, gargalhadas e tanto mais que fica por escrever. Gostaria também de agradecer às mestres Maria Morais e Margarida Rodrigues por toda a ajuda em ambiente de laboratório, ao Dr. Nuno Costa pelas análises de morfologia dos aerogéis e à rede PT-NMR por me facultar o acesso aos espectrómetros.

Um especial obrigado ao Cenimat|I3N e ao DCM por tudo o que me proporcionaram ao longo dos últimos 5 anos, sou grato por todas as amizades que pretendo levar em diante. As memórias de tantos dias passados aqui, tantos momentos que levarei no coração para a vida inteira.

O mais especial dos agradecimentos é e sempre será aos meus pais, duas pessoas tão únicas, sempre dispostas a fazer tudo o que estiver e não estiver ao seu alcance para que eu cumpra os meus sonhos, obrigado Nonõ por seres minha irmã e me ensinares tanto, espero que seja assim a vida inteira.

Obrigado, prima Carolina, por teres sido um pilar fundamental ao longos destes últimos 9 meses, por estares sempre disponível para me ouvir, por verificares sempre se já tinha acordado e não ia chegar atrasado à faculdade, por ires jantar comigo aos mais diversos restaurantes cada vez que o dia não me tinha corrido assim tão bem. És muito especial para mim.

Por último quero agradecer aos amigos que a faculdade me trouxe: Francisca, Miguel, Daniel, Tomás, Ana e aos meus afilhados Guilherme, Carolina, Catarina e Carolina.

Sem tudo isto, a faculdade não teria sido o mesmo, OBRIGADO.

"The only limit to our realization of tomorrow will be our doubts of today."

(Franklin D. Roosevelt)

ABSTRACT

Nowadays, society faces several challenges, with rising CO_2 levels in the atmosphere. Chitosan aerogels are promising for catalysis, drug delivery, and environmental remediation. However, improving their catalytic, mechanical, and textural properties presents challenges. This dissertation investigated the development of chitosan-based aerogels incorporating ionic liquids (ILs) and poly(ionic liquids) (PILs) with surface active properties to optimize their structural stability and porosity.

Imidazolium-derived ILs and a PIL were synthesized with yields over 92%. These were then used to develop aerogels, using several formulations, varying IL and PIL concentrations, crosslinkers, and starch addition. Nitrogen adsorption studies showed that both ILs and PIL significantly impacted their shrinkage, density, and textural properties. Scanning electron microscopy revealed noticeable changes in fiber architecture and arrangement. Higher concentrations of PIL caused increased shrinkage due to denser crosslinking, while starch helped to counteract this effect by acting as a reinforcing agent. Solid-state Nuclear Magnetic Resonance and Attenuated Total Reflectance Fourier-Transform Infrared analyses confirmed the successful incorporation of ILs and PIL.

The aerogels were used in cycloaddition reactions of epoxides to CO_2, resulting in cyclic carbonates with up to 70% yields. Thermal treatment improved the catalytic efficiency of the PIL-based aerogels, underscoring the importance of processing conditions.

Keywords: Surfactant Ionic liquids, Aerogels, Chitosan, CO_2 Conversion.

RESUMO

Atualmente, a sociedade enfrenta vários desafios, incluindo o aumento dos níveis de CO_2 na atmosfera. Os aerogéis de quitosano são promissores para catálise, libertação controlada de medicamentos e recuperação ambiental. No entanto, melhorar as suas propriedades catalíticas, mecânicas e texturais apresenta desafios. Esta dissertação investigou o desenvolvimento de aerogéis à base de quitosano incorporando líquidos iónicos (LIs) e poli(líquidos iónicos) (PLIs) com propriedades de superfície ativa para otimizar a sua estabilidade estrutural e porosidade.

Foram sintetizados LIs e PLI derivados de imidazólio com rendimentos superiores a 92%. Estes foram utilizados para desenvolver aerogéis, com várias formulações, variando as concentrações de LI e PLI, reticulantes e a adição de amido. Estudos de adsorção de azoto mostraram que tanto os LIs quanto o PLI impactaram significativamente a contração, densidade e propriedades texturais dos aerogéis. A microscopia eletrónica de varrimento revelou mudanças notáveis na arquitetura e organização das fibras. Maiores concentrações de PLI causaram maior contração devido à reticulação mais densa, enquanto o amido ajudou a mitigar esse efeito, atuando como agente de reforço. Análises de Ressonância Magnética Nuclear em estado sólido e de Infravermelho com Transformada de Fourier de Refletância Total Atenuada confirmaram a incorporação bem-sucedida dos LIs e PLI.

Os aerogéis foram utilizados em reações de cicloadição de epóxidos com CO_2, resultando em carbonatos cíclicos com rendimentos de até 70%. O tratamento térmico melhorou a eficiência catalítica dos aerogéis à base de PLI, destacando a importância das condições de processamento.

Palavras-chave: Líquidos iónicos surfactantes, Aerogéis, Quitosano, Conversão CO_2.

CONTENTS

LIST OF FIGURES

LIST OF TABLES

ABBREVIATIONS

AIBA	2,2'-Azobis(2-methylpropionamidine) Dihydrochloride
ATR-FTIR	Attenuated Total Reflectance - Fourier Transform Infrared Spectroscopy
BET	Brunauer-Emmett-Teller
CAC	Critical Aggregation Concentration
CHT	Chitosan
CP-MAS	Cross-Polarization Magic Angle Spinning
DMSO	Dimethyl Sulfoxide
eCO2RR	Electrocatalytic CO_2 Reduction
EGDE	Ethylene Glycol Diglycidyl Ether
EtOH	Absolute Ethanol
ILs	Ionic liquids
NMR	Nuclear Magnetic Resonance
PILs	Poly(Ionic liquid)s
PRE	Pre-treatment
SAILs	Surface-Active Ionic Liquids
SC	Supercritical

SCD	Supercritical Drying
SEM	Scanning Electron Microscopy
SF-Cu/CA	Silk Fibroin-derived Carbon Aerogels
STR	Starch
TLC	Thin layer chromatography

1

INTRODUCTION

1.1 Ionic Liquids and Poly(Ionic Liquid)s

Ionic liquids (ILs) have gained significant attention for their unique physicochemical properties and diverse applications. Research efforts highlight the strong relationship between their nanometric-scale structural organization and macroscopic properties, such as viscosity, diffusion, and conductivity. This interplay has opened new avenues for their use, with studies confirming that their physical and chemical properties are intrinsically tied to their structural organization [1].

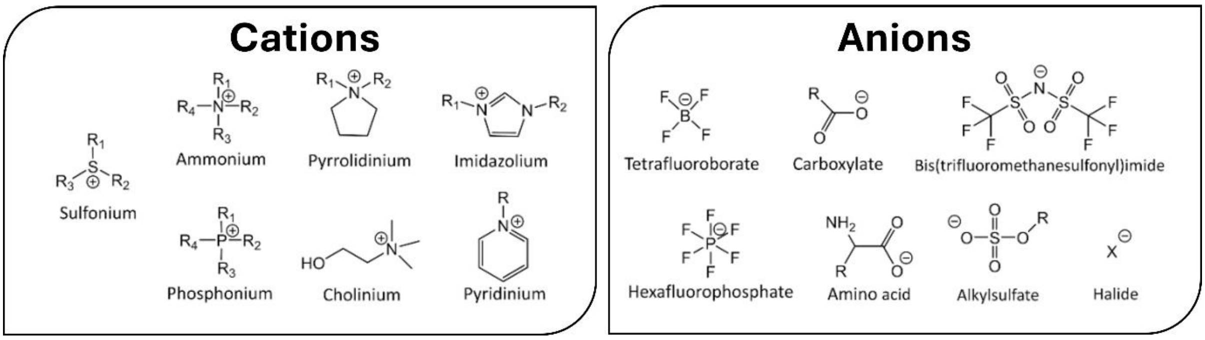

Figure 1 Typical ions in ILs adapted from [1].

ILs are organic salts composed of organic cations and organic or inorganic anions with melting points below 100 °C. As their name implies, these materials are exclusively made up of ions. The most common type is imidazole ILs with low viscosity [2]. In Figure 1, some examples of common IL cations and anions can be observed.

ILs possess highly desirable properties, such as high thermal stability, non-volatility, good conductivity, and non-flammability. In terms of applications, ILs can be employed in the synthesis of organic and inorganic materials, electrochemistry, separation technologies, and materials science [3]. Besides, ILs also find application in membrane technologies. Recently, some ILs have been studied for their ability to increase permeability by 400% when incorporating non-polymerizable ILs at relative percentages close to 20 mol% of free ILs. This advancement opens new possibilities for the use of ILs in membrane technologies and separation processes [4].

Poly(ionic liquid)s (PILs), also known as polymerized ILs, are a unique type of polyelectrolyte where each repeating unit in the polymer chain contains an IL component. These IL units are linked together by a polymer backbone, creating a large-scale molecular structure [5]. Incorporating the properties of ILs, such as ionic conductivity, chemical resistance, thermodynamic stability, and customizable design into PILs has led to groundbreaking applications across various industries, such as water purification, solar cells, drug delivery, or even electrical energy storage [6], [7]. Due to their high conductivity, wide electrochemical stability, excellent thermal stability, and good chemical resistance, PILs are widely used as solid electrolytes in various electrochemical devices [8]. Additionally, ILs have garnered significant attention for their ability to capture and store CO_2, particularly because of their selectivity for CO_2 at ambient temperature. This unique characteristic positions ILs as a promising solution for carbon capture, making them highly relevant in the fight against climate change. Both PILs and ILs showcase exceptional potential in advanced technological applications due to their diverse properties [9]. In Figure 2, a pictorial representation of PIL structures is presented.

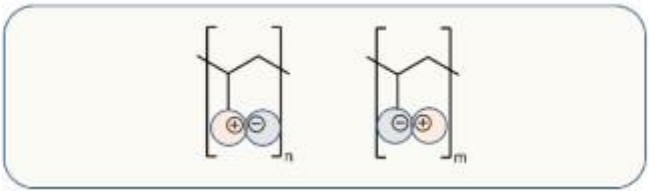

Figure 2 Pictorial representation of poly(ionic liquid)s (PILs) with cationic and anionic backbones adapted from [10].

Certain combinations of ILs can exhibit low viscosity values. However, viscosity can be modulated by substituting, for instance, a $-CH_3$ group with an $-NH_2$ group. This results in an increase in density (by about 10% compared to the experimental value) and a considerable reduction in molar volume. This alteration leads to an increase in the IL's viscosity, illustrating how structural changes are reflected in property changes [10].

In CO_2 capture under high pressure and temperature conditions, viscosity predictably becomes less of a critical factor as its value decreases significantly. However, this also leads to a reduction in performance [9].

ILs and PILs share several characteristics with surfactants, including their ability to reduce surface tension. Their ionic and tuneable nature allows them to be used as complementary agents to traditional surfactants.

1.2 Surfactants

Surfactant entities possess molecular structures with both hydrophobic and hydrophilic properties, making them amphiphilic compounds. Surfactants can be classified into four main types: anionic, cationic, amphoteric, and non-ionic [11].

- **Anionic Surfactants:** These surfactants have a hydrophilic part with a negative charge.
- **Cationic Surfactants:** The hydrophilic part carries a positive charge in these surfactants.
- **Amphoteric Surfactants:** These surfactants have a hydrophilic part that is simultaneously positively and negatively charged.
- **Non-Ionic Surfactants:** These surfactants have a neutral hydrophilic part.

Surface active ionic liquids (SAILs) exhibit excellent surfactant properties, recognized for their ionic nature, low critical aggregation concentration (CAC), and the ability to form various types of nano-aggregated micelles and liquid crystalline phases [12]. In most common SAILs, the hydrophobic component is incorporated into the cation, making them quite like cationic surfactants. The main difference between SAILs and traditional surfactants lies in their melting points, which are below 100 °C, as well as their functional attributes, such as high solubility in aqueous media, liquid behavior, tuneable nature, and surface activity [3]. SAILs have the capability to reduce the interfacial tension between liquid-liquid and liquid-air systems, demonstrating superior performance compared to conventional surfactants. By combining the properties of surfactants with those of ILs, we enhance their ability to withstand high temperatures, a characteristic inherent to ILs [11].

In addition to lowering interfacial tension, SAILs are stable and resilient surfactants with a low environmental impact, as they are recyclable. This has garnered significant interest from researchers [11]. Figure 3 presents a pictorial view of the amphiphilic structure of SAILs.

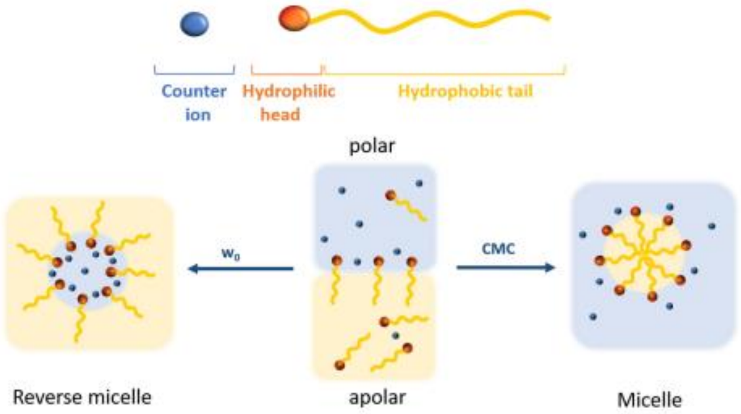

Figure 3 Pictorial view of the amphiphilic structure of SAILs [13].

ILs, PILs, and surfactants play critical roles in aerogels' synthesis, functionalization, and application. They help to control the pore structure, surface chemistry, and mechanical properties of aerogels, enabling the creation of advanced materials with enhanced functionality. The integration of ILs, PILs, or surfactants into aerogel systems opens possibilities in fields like energy storage, environmental remediation, catalysis, and advanced sensing technologies [14][15].

1.3 Aerogels

Aerogels belong to a class of nanoporous materials that are created by removing fluids from the pores of gels without causing significant damage to their polymeric network structure. Aerogels are characterized by their high porosity, low density, large specific surface area, excellent absorption capacity, high electrical conductivity, and stable physicochemical [16][17]. Their applications are diverse, ranging from thermal insulation and separation of mixtures, such as water and oil, to catalytic processes or even biomedical processes [18][19].

Aerogels are obtained from alcogels by removing the ethanol present in the structure using supercritical (SC) CO_2 drying without causing damage. As a result, aerogels with high porosity, low density, and high capacity for CO_2 capture on their surface are obtained [20]

In our research group, we have successfully developed *AEROPILs*, which are PIL-based aerogels and used them for CO_2 capture and conversion [20]. The key objective of this thesis is to extend this concept by incorporating surfactant-based PILs supported on aerogels, producing *AEROSAILs*. This combination aims to be effective and successful by leveraging the CO_2 absorption properties of PILs, which provide CO_2 affinity, and the added stability provided by surfactants. Additionally, this solution offers low cost, ease of large-scale production, and environmentally friendly technology [21]. By combining the properties of aerogels with the functionalities of ILs, we aim to take advantage of the solid state, which will provide high performance in CO_2 capture due to its porosity. Integrating surfactant-based PILs with aerogels is expected to significantly enhance CO_2 absorption capacity in most cases while allowing control over the porosity, directly influencing absorption capacity.

The formulation of aerogels with PILs exhibits high selectivity that can be tailored to the CO_2 molecule. A literature review revealed that, in terms of performance, cations derived from ammonium show the best results, followed by pyridinium, phosphonium, and imidazolium. For anions, acetates are the most effective in promoting CO_2 absorption, followed by tetrafluoroborate, hexafluorophosphate, and bis(trifluoromethylsulfonyl)imide [20].

Table 1 presents different porous materials and their respective CO_2 capture values according to their specific surface area.

Table 1 A comparison of CO_2 capture capacities and the corresponding specific surface areas reported for various bio-based sorbents.

Entry	**Material**	**Modifications**	**n_{CO2} (mmol g$^{-1)}$**	**S_{BET} (m^2/g)**	***P* (bar)**	**T (ºC)**	**Ref.**
1	Pure chitosan	-	0.02	nd	nd	nd	[20]
2	CHT-GO aerogels	CHT grafted GO	0.26	33.32	1.00	25	[20]
3	CHT-GO-20%	CHT-GO aerogels	4.15	412.00	1.00	25	[20]
4	QCHT/PVA aerogels	Quaternized CHT+ PVA	0.18	nd	nd	20	[20]
5	CHT-TPPS	Ionic complexation	0.90	26,75	5.00	25	[20]
6	COF-IL@CHT aerogel	COF-CHT aerogel + allylimidazolium IL	1.05	103.30	1.00	25	[20]
7	40%([EMIM][OAc] + 5%CHT) +60% silica	SILP—encapsulation of ionogel with nanoporous fumed silica	0.71	53.00	1.00	40	[20]
8	40%([BMIM]Cl + 5%CHT) +60% silica		0.11	52.00	1.00	40	[20]
9	Coconut shell	Carbonization	1.00	1459.00	3.00	25	[22]
10	Phenol-formaldehyde resin and olive stones (20:80 wt%	Carbonization	2.3	1233.00	1.20	25	[23]
11	Shrimp Shells	Chemical KOH activation	4.2	1984.70	1.00	25	[24]

1.4 CO_2 Conversion

The CO_2 capture and conversion process is crucial in developing this thesis. By converting the captured CO_2, we can repurpose it into value-added compounds for industry, further mitigating its environmental impact [4].

Various solutions, such as Ag-Cu aerogels, exist in the literature for electrochemical CO_2 conversion to CO. In this case, the strategy for electrocatalytic CO_2 reduction (eCO_2RR) uses Ag-Cu bimetallic aerogels to lower overpotential and improve selectivity, enhancing catalyst performance [25]. Additionally, a self-assembly approach has been developed using silk fibroin-derived carbon aerogels (SF-Cu/CA) with copper nanoparticles, achieving high current density, Faraday efficiency, and long-term stability, further demonstrating the potential of metal-carbon matrix catalysts in CO_2 electroreduction [26].

To achieve CO_2 conversion, aerogels can be used, as demonstrated previously by our team [27]. However, ILs can be used in various ways, such as in preparing N-doped porous carbons, which subsequently act as adsorbents and catalysts in the conversion reaction. The rate of CO_2 conversion can be influenced by several factors, with pressure being the most significant, followed by temperature, reaction time, and added solvents [4].

PILs can form structures and morphologies that are impossible with conventional ILs, making them valuable allies in CO_2 conversion. By modifying their molecular structure, their properties, including CO_2 selectivity, can be enhanced, leading to better conversion performance and greater stability [4].

According to a review previously reported by our research group, when evaluating CO_2 conversion into cyclic carbonates using ammonium-derived ILs as catalysts, it was found that the presence of hydroxyl groups generally improves CO_2 conversion performance. The study also revealed that the conversion rate varies depending on the cation used, with the following order of effectiveness: imidazolium > ammonium > diazabicycloundecenium > phosphonium [4]. Most CO_2 conversion catalysts exhibit conversion rates exceeding 70%, with some reaching up to 100% in certain cases. The selectivity for CO_2 is around 90%, depending on various pressure and temperature conditions [4].

2

MATERIALS AND METHODS

The materials used in this dissertation can be found In Appendix A1 and the characterizations in Appendix A2.

2.1 ILs and PIL Synthesis

2.1.1 Decanopropylimidazolium Bromide Synthesis

To synthesize decanopropylimidazolium bromide (**IL1,** Figure 4), 0.5 ml of 1-(3-aminopropylimidazole) and 0.85 ml of 1-bromodecane were added to a round bottom flask. The solution was heated to 70 °C, under stirring for 2 days, until the consumption of the 1-3(-aminopropylimidazole) was detected. To verify the completion of the reaction, thin-layer chromatography (TLC) was performed. The resulting mixture was then subjected to vacuum, yielding a solid, and yellowish product. The yield of this reaction was 97%.

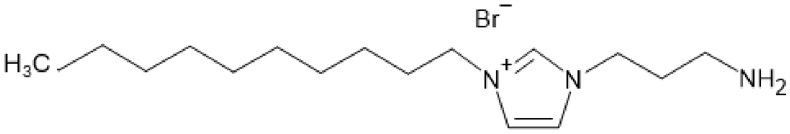

Figure 4 Chemical structure of decanopropylimidazolium bromide (**IL1**).

2.1.2 Decylvinylimidazolium Bromide Synthesis

For the synthesis of the 1-decyl-3-vinylimidazolium bromide (**IL2,** Figure 5), 2.4 ml of 1-vinylimidazole, 5.4 ml of 1-bromodecane, and 2.5 ml of methanol were added to a round bottom flask. The mixture was heated to 60 °C, under stirring for 2 days. Similar to the previous reaction, TLC confirmed the complete conversion. The mixture was then subjected to vacuum, resulting in a yellow-colored substance with an oily texture. The yield of this reaction was 92%.

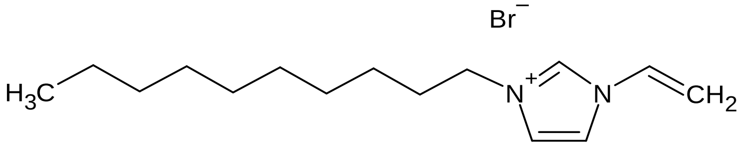

Figure 5 Chemical structure of 1-decyl-3-vinylimidazolium bromide (**IL2**).

2.1.3 PIL Synthesis

The poly(decylvinylimidazolium bromide) was synthesized according to a previously reported procedure [28]. Briefly, 2.4 g of 1-decyl-3-vinylimidazolium bromide was dissolved in 50 mL of water in a 250 mL round bottom flask. The monomer solution was mixed with 24 mg of initiator (AIBA). The mixture was completely deoxygenated by five cycles of the freeze-pump-thaw procedure and then kept for several hours under magnetic stirring at 250 rpm. Subsequently, the mixture was continuously stirred at 75 °C in an oil bath overnight. After cooling down, the final colloid dispersion was exhaustively dialyzed using a 14 kDa membrane against deionized water until the conductivity of water was below 3 μS/cm.

2.2 Preparation of Chitosan Aerogel Beads - *AEROSAILs*

2.2.1 Preparation of Chitosan Hydrogel

The chitosan hydrogel particles were prepared according to the sol-gel method previously described [29]. The first step was to dissolve the chitosan (2.5% w/v) in Milli-Q water with an acetic acid solution (1% w/v), obtaining 30 mL of total solution volume. When the chitosan was completely dissolved, solutions of IL (30% and 50% w/w related to chitosan) and PIL (7.5% and 15% w/w related to chitosan) were added. Starch (10% w/w relative to chitosan) was added in specific samples.

The IL and PIL were dissolved in an aqueous solution (3 mL), and the respective volume was subtracted from the total volume of the acetic acid chitosan solution. The chitosan solutions were prepared with EGDE (32% w/w related to chitosan) as a crosslinker and stirred for 15 minutes while heated (50 °C) to avoid the leakage of the IL and PIL according to a previously described procedure [27]. activating the crosslinker. We also produced chitosan solutions with different loadings of IL and PIL, with and without EGDE as a crosslinker and starch. Subsequently, the chitosan solution with a range of 22-25 mL was transferred to a plastic syringe (with a nozzle diameter of 2 mm) and added dropwise to 100 mL of water and NaOH 1 mol/L solution, and hydrogel beads were formed. These beads were left in the gelation bath for 2 hours. For comparison, beads without PIL, IL, EGDE, and starch were produced similarly.

2.2.2 Solvent exchange

The gelation bath containing the gel beads was poured out of the beaker and immediately replaced with 100 mL of absolute ethanol (EtOH). After 4 hours, a second solvent exchange with an equivalent volume of EtOH was performed to ensure the removal of any residual water from the gel particles.

2.2.3 Supercritical extraction of the alcogel solvent

The alcogel particles were loaded into Whatman paper cartridges and placed inside the 300 mL high-pressure cell of the supercritical drying (SCD) apparatus. To prevent premature evaporation of the solvent within the alcogels before achieving supercritical conditions, 75 mL of ethanol was introduced into the vessel. The high-pressure cell was then subjected to a flow of $scCO_2$ while maintaining a constant pressure of 120 bar and a temperature of 40 °C for 2 hours. Subsequently, the cell was maintained in batch mode at the same temperature and pressure for an additional hour. Finally, a second flow cycle was carried out, identical to the initial one but for a shorter duration of 30 minutes to 1 hour, and the cell was slowly depressurized.

2.3 Batch catalytic cycloaddition of CO_2 to epoxides

In a typical experiment, 1 mL of the epoxide (butylene oxide or epichlorohydrin substrate and 100 mg of the aerogel beads were added to a stainless-steel reactor (45 mL) and flushed with CO_2 three times. Prior to the reaction, the aerogel beads underwent a pretreatment process involving washing with diethyl ether followed by vacuum drying. This pretreatment aimed to create new active sites by removing impurities or trapped substances, such as structural water. The reactor was then stirred under a 10 bar CO_2 atmosphere at 135 °C for 72 h. The yield was determined through the analysis of ^{1}H NMR spectra of the crude mixture.

The pre-treatment (PRE) of the aerogels was introduced before some of the catalytic processes. Briefly, for the recycling process, the AEROSAILS beads were thoroughly washed twice with diethyl ether and then dried under moderate vacuum at 60 °C for a minimum of 48 hours before being reused in CO_2 conversion reactions. This procedure was employed before each catalytic cycle in the recycling studies.

3

RESULTS AND DISCUSSION

In this dissertation, chitosan-based aerogels incorporating surface active ILs and PILs were produced and evaluated for their structural and catalytic properties. Several ILs and a PIL with surface active properties were synthesized and characterized. The subsequent production of chitosan-based aerogels incorporating ILs and PILs and the respective characterization aimed to investigate how IL, PIL, and different crosslinking/processing conditions affect the aerogels' structure, surface area, and catalytic properties. Attenuated Total Reflectance - Fourier Transform Infrared Spectroscopy and NMR spectroscopy were used to study the IL/PIL incorporation. Nitrogen adsorption-desorption analysis was employed to evaluate how IL/PIL and heat treatment modify surface areas, and SEM was used to observe how PIL altered aerogel fiber architecture. The aerogels were tested for catalytic activity in CO_2 cycloaddition reactions.

3.1 Synthesis and characterization of IL and PIL

After synthesizing **IL1** and **IL2**, which yielded 97% for **IL1** and 92% for **IL2**, we proceeded with their analysis using NMR and ATR-FTIR techniques, with the corresponding spectra shown subsequently. For a better understanding, we start by introducing the reactions that lead to the formation of **IL1** (Figure 6) and **IL2** (Figure 7), respectively.

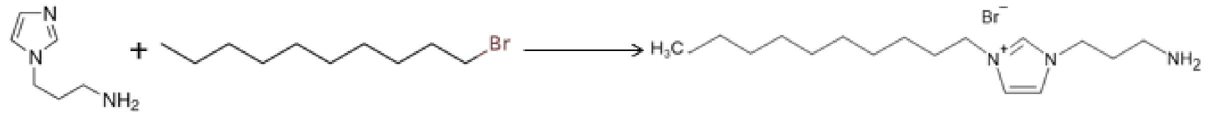

Figure 6 Synthesis of **IL1**.

The synthesis reaction of **IL2** is represented in Figure 7.

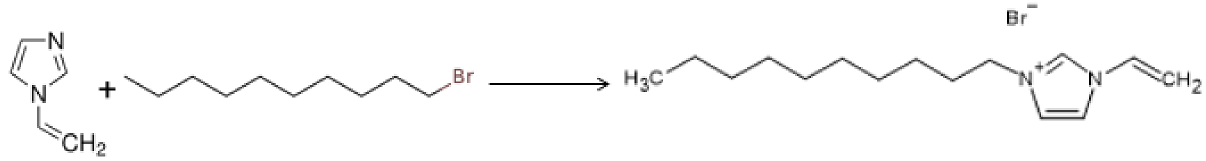

Figure 7 Synthesis of **IL2**.

The polymerization of the **IL2** is represented in Figure 8. This reaction was carried out using a monomer concentration of 0.048g/L in water, where **IL2** is in its critical micelle concentration (CMC=48mg/mL), as described in [28]. As a result, the product aggregates and then polymerization takes place.

Figure 8 Synthesis of PIL.

Figure 9 shows the ATR-FTIR spectra of **IL1** and **IL2** which show several characteristic features that help identify the two ionic liquids. Both ILs exhibit bands in the 1400-1600 cm^{-1} range, corresponding to C=N and C=C stretching vibrations in the imidazolium ring. Additionally, vibrations associated with aromatic C-H stretching are observed between 3100 and 3300 cm^{-1} in both **IL1** and **IL2**, which are more pronounced in **IL2**.

A significant difference is noted around 3400 cm^{-1}, where **IL1** shows a distinct band due to the N-H stretching vibration of the NH_2 group. The band around 1650 cm^{-1} can be attributed to the vinylic C=C represented of **IL 2** [30].

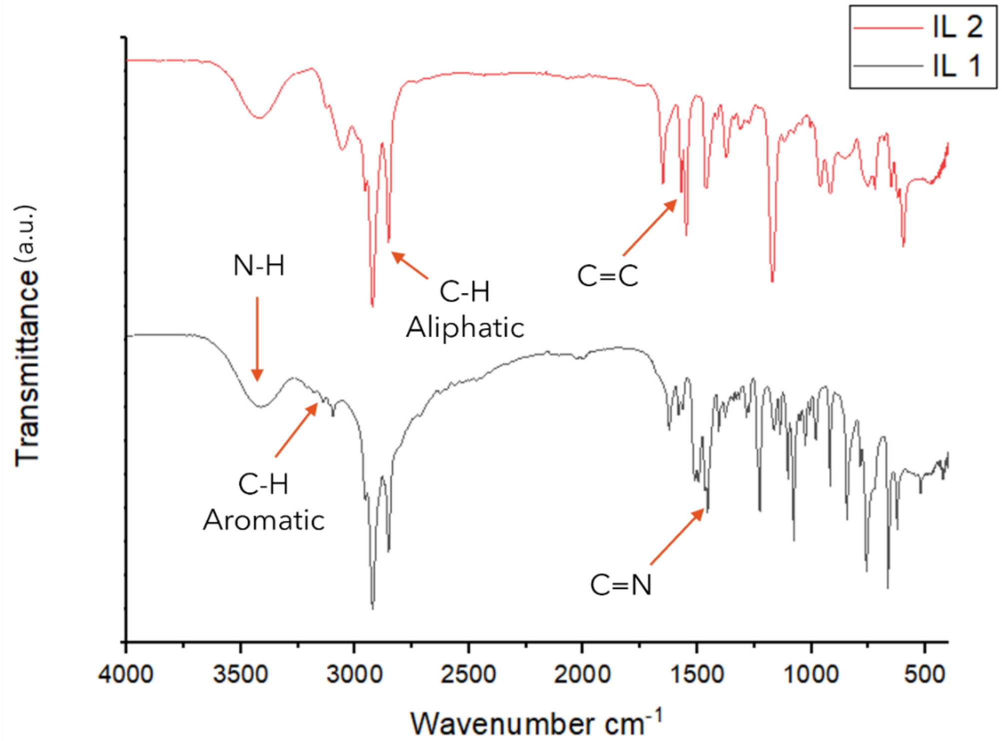

Figure 9 ATR-FTIR spectra of IL1 and IL2.

Upon analyzing the spectra of the polymerized ionic liquid (PIL) in Figure 10, it is evident that the characteristic bond of the **IL2** C=C, which was originally represented in the range of 1644 cm^{-1}, is no longer present in the PIL spectra due to the polymerization process. Compared to the spectrum of **IL2**, the polymer spectrum may display broader bands or fewer sharp features, indicative of a more amorphous structure and the loss of distinct molecular vibrations due to crosslinking.

The spectrum suggests that polymerization has altered the structural characteristics of **IL2**, leading to the formation of a more complex network. The analysis confirms that polymerization has successfully transformed the IL into a polymeric material.

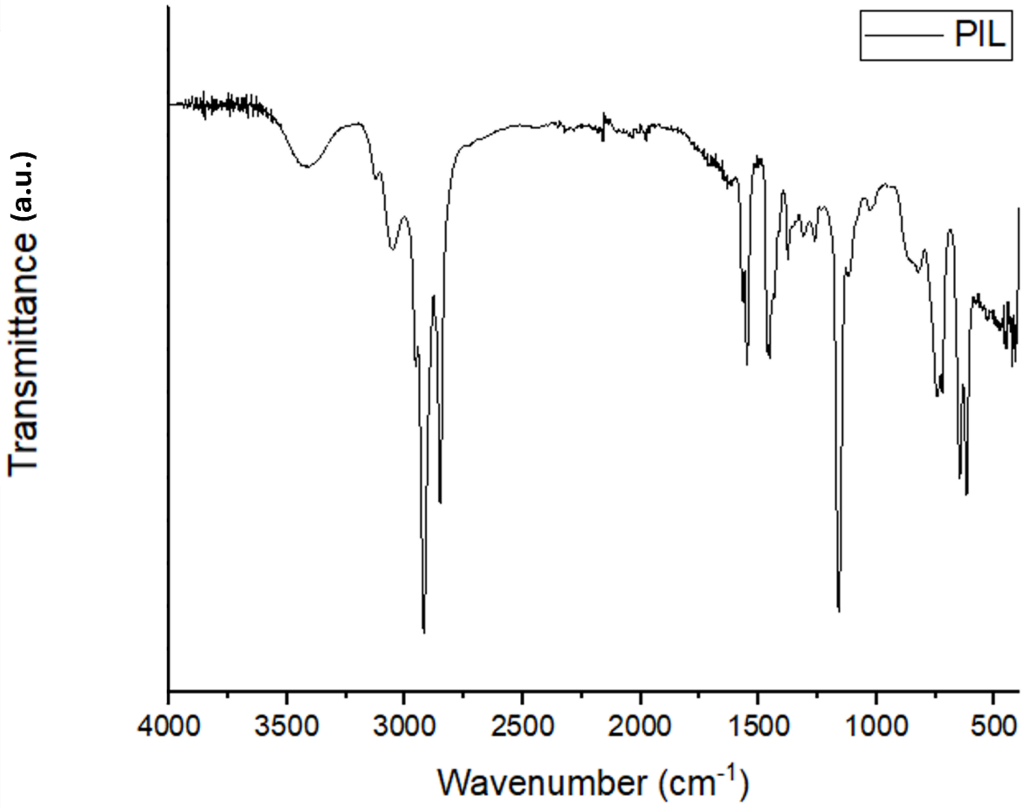

Figure 10 ATR-FTIR Spectra of PIL.

IL1 exhibited very low solubility in the common deuterated solvents. Therefore, the respective NMR analysis was performed in solid-state. Figure 11 presents the ^{13}C CP-MAS NMR spectrum of **IL1**. The methyl group (**C(15)**H_3) attached to the alkyl chain is likely resonating 15 ppm, while the long chain of methylene groups (**C(7-13)**H_2) corresponds to the signals between 20 to 32 ppm as each peak corresponds to the repeating methylene units along the alkyl chain. The carbons in the imidazole ring, numbered **(C2, C4 and C5)** resonate between 120 to 135 ppm. Here, the presence of a fourth signal may indicate some product contamination. The methylene adjacent to the amine in the propylamine side chain corresponds to the peaks that resonate around 40 ppm (**C(18)**H_3). It is important to note that the asterisks indicate the spinning sidebands in the NMR spectrum.

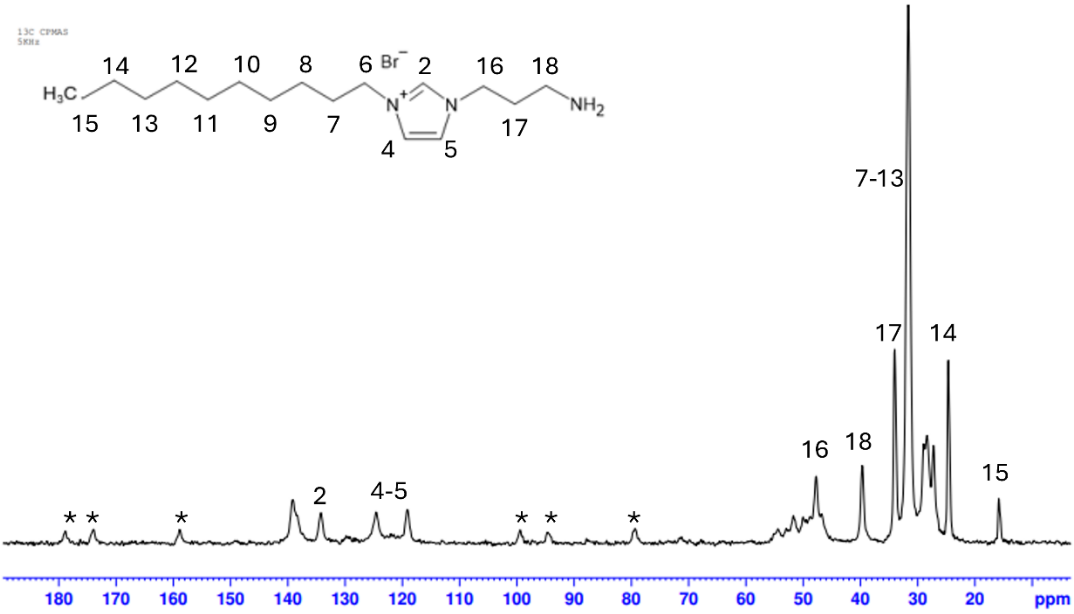

Figure 11 ^{13}C CP-TOSS NMR spectra of **IL1**.

In the ^{1}H-NMR spectrum of **IL2** shown below, the peak around 0.5 ppm corresponds to the methyl group protons (**H15**). The subsequent peak, around 1.2 ppm, corresponds to methylene protons (**H8-H14**). The peak at approximately 1.9 ppm is associated with the **H7** nuclei, while the peak around 4.3 ppm refers to the proton next to the imidazolium ring **(6)**. The peaks at 5.5, and 6 ppm, relate to the double bond nuclei **H17**, and at 7.2 ppm resonates proton **H16**. The methylene group (**H6**) next to the aromatic ring resonates at 5.0 ppm. Finally, the aromatic protons H4 and H5 present chemical shifts between 7.6-7.9 ppm.

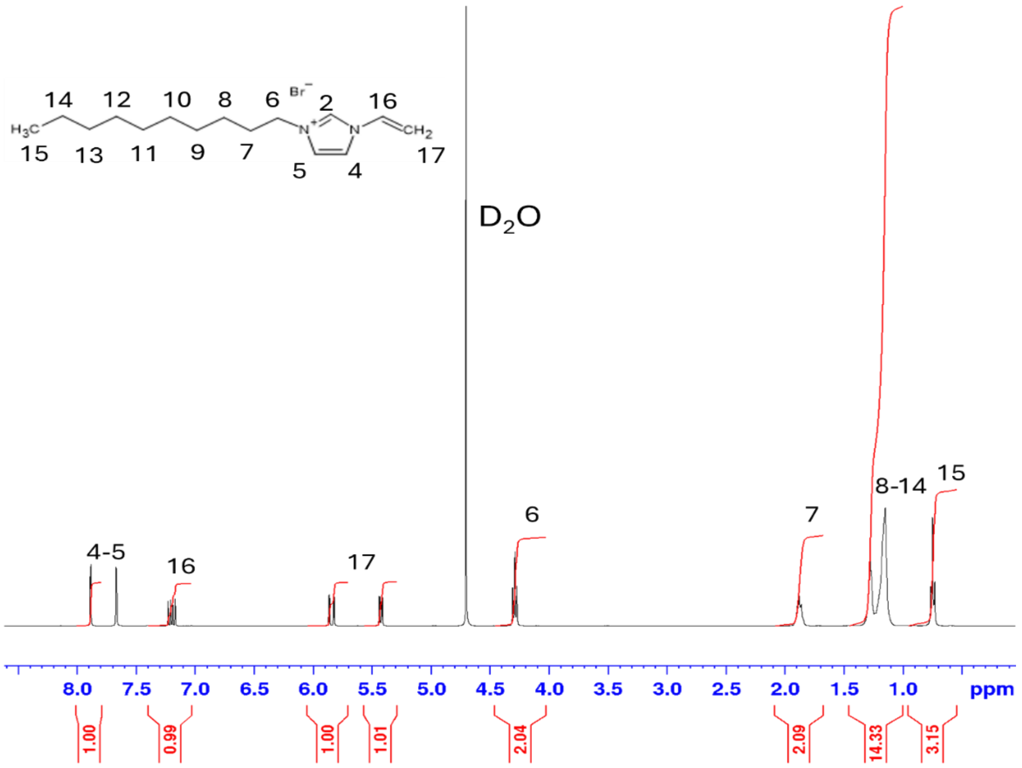

Figure 12 ^{1}H-NMR spectrum of **IL2** in D_2O.

3.2 Synthesis and characterization of *AEROSAILs*

In the present work, aerogels were produced with surface active ILs and PILs, Introducing several changes com compared to previous reports of the group [20]. The following table provides a detailed overview of each samples' composition. The first sample contains only chitosan (**CHT**$_{2.5\%}$), a reference for comparison with the subsequent samples. In entry 7, the sample contains only PIL, without the crosslinker, to allow an understanding of PILs effect on our sample´s crosslinking.

The amount of chitosan was adjusted, starting with chitosan at 2.5% (w/v) and subsequently reduced to 2.0% (w/v) in sample 11 and 1.5% (w/v) in sample 10 to allow a higher percentage of incorporated PIL. In two of the samples (entries 6 and 12), labelled as "STR10%", indicating the addition of starch (10% w/w) relative to chitosan, starch was added to evaluate its interaction with chitosan in the incorporation of IL and PIL. EGDE (32% w/w) was only included in specific samples labeled "EGD32%" to indicate its presence. "IL" and "PIL" refer to the presence of ionic liquid or poly(ionic liquid), along with their respective percentages.

Table 2 Composition of aerogels.

Entry	Sample	Chitosan (mg)	Starch (mg)	EGDE (µL)	IL1 (%w/w)	PIL (%w/w)
1	**CHT$_{2.5\%}$**	750	-	-	-	-
2	**CHT$_{2.5\%}$:EGD$_{32\%}$**	750	-	200	-	-
3	**CHT$_{2.5\%}$:EGD$_{32\%}$:T>50ºC**	750	-	200	-	-
4	**CHT$_{2.5\%}$:EGD$_{32\%}$:IL1$_{30\%}$**	750	-	200	30	-
5	**CHT$_{2.5\%}$:EGD$_{32\%}$:IL1$_{50\%}$**	750	-	200	50	-
6	**CHT$_{2.5\%}$:STR$_{10\%}$:EGD$_{32\%}$:IL1$_{50\%}$**	675	75	200	50	-
7	**CHT$_{2.5\%}$:PIL$_{15\%}$**	750	-	-	-	15
8	**CHT$_{2.5\%}$:EGD$_{32\%}$:PIL$_{7.5\%}$**	750	-	200	-	7.5
9	**CHT$_{2.5\%}$:PIL$_{7.5}$**	750	-	-	-	7.5
10	**CHT$_{1.5\%}$:EGD$_{32\%}$:PIL$_{50\%}$**	450	-	144	-	50
11	**CHT$_{2.0\%}$:EGD$_{32\%}$:PIL$_{50\%}$**	600	-	192	-	50
12	**CHT$_{2.5\%}$:STR$_{10\%}$:EGD$_{32\%}$:PIL1$_{50\%}$**	675	75	200	-	50

Some aerogel samples were selected for solid-state NMR analysis to elucidate the obtained structure. **CHT:EGD$_{32\%}$:PIL$_{7.5\%}$** was chosen to analyze an aerogel containing PIL; **CHT:EGD$_{32\%}$:IL1$_{50\%}$** to observe the presence of **IL1**; **CHT$_{2.0\%}$:EGD$_{32\%}$:PIL$_{50\%}$** was selected as an example with a reduced amount of chitosan, which was needed to control the viscosity increase when incorporating PIL; and finally two aerogels containing starch, one with incorporated PIL (**CHT$_{2.5\%}$:STR$_{10\%}$:EGD$_{32\%}$:PIL1$_{50\%}$**) and the other with incorporated **IL1** (**CHT:STR$_{10\%}$:EGD$_{32\%}$:IL1$_{50\%}$**), all the samples contain the crosslinker EGDE.

Chitosan is a linear polysaccharide composed of D-glucosamine (deacetylated unit) and N-acetyl-D-glucosamine (acetylated unit). It has hydroxyl groups (-OH) attached to the sugar rings and amino groups (-NH$_2$) on the glucosamine units, making it a derivative of chitin (Figure 13).

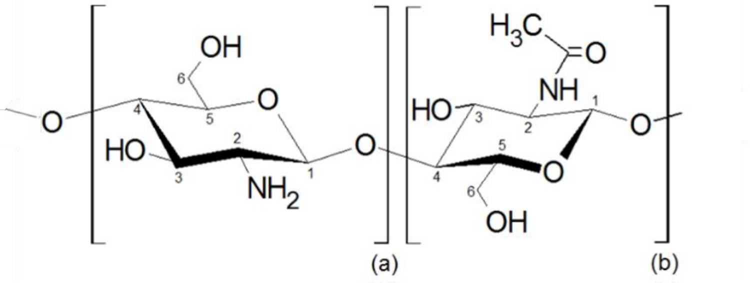

Figure 13 Chemical structure of the chitosan molecule (a>74%).

After examining the ^{13}C CP-MAS NMR spectra below (Figure 14), it is possible to observe at 165-170 ppm a chemical shift related to the C=O of chitosan; the resonance of the imidazolium groups is observable between 120 and 140 ppm in all spectra [18]. This observation supports the successful immobilisation of IL and PIL in the aerogels. As for the chemical shifts between 50 and 110 ppm, these signals are characteristic of the chitosan backbone, that overlaps with starch, whenever present. C1 nuclei resonate around 100 ppm, while the other carbon atoms present chemical shifts between 60 and 80 ppm. The carbon atom from the -CH_2OH (C-6) group can be observed around 60 ppm [31]. In the range around 22 ppm, there is a chemical shift common to all the samples belonging to chitosan, specifically to the methyl from chitosan's acetyl group. The resonances between 30 and 50 ppm belong to the PIL and IL side chains [32]. A complete version of each spectra separated is showed in the appendix.

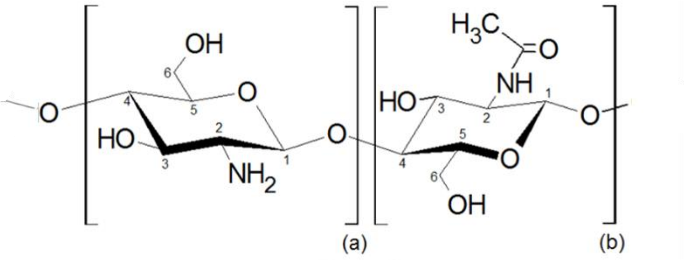

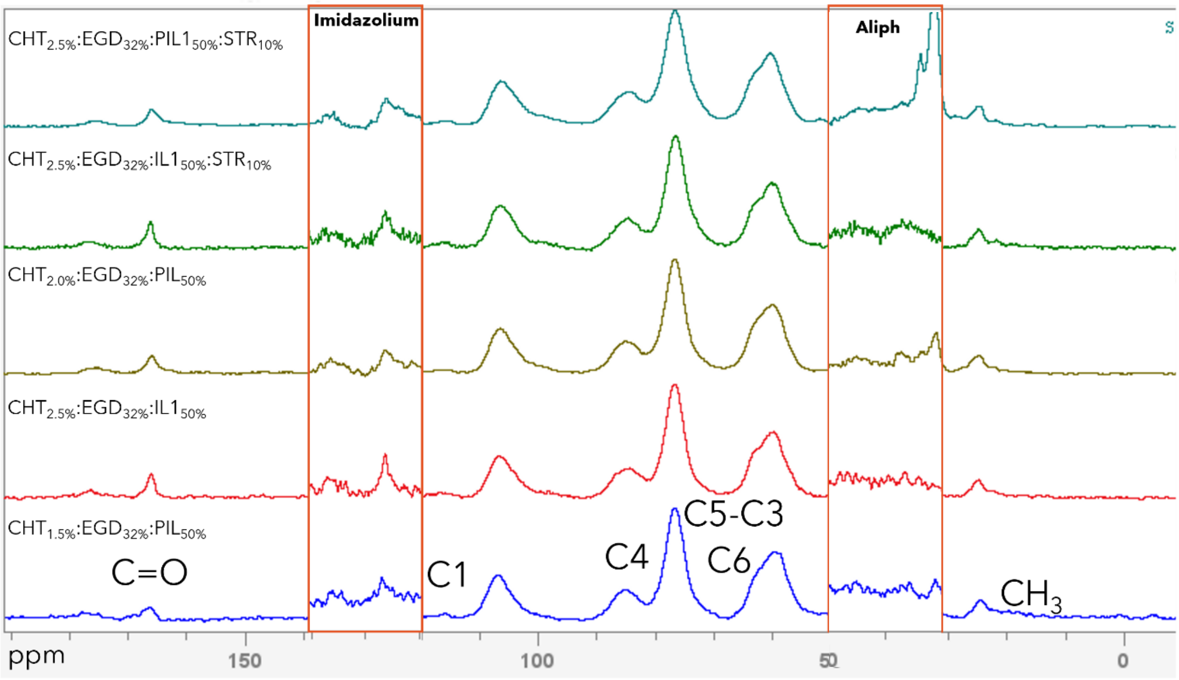

Figure 14 ^{13}C-CP TOSS NMR spectra of aerogels.

The ATR-FTIR spectra comparison in Figure 15 illustrates the interaction between pure chitosan aerogels, crosslinked chitosan aerogels, PIL-incorporated *AEROSAILs*, and IL-incorporated aerogels (Panels A and B), respectively.

In Figure 15.A it is possible to observe the distinct vibrations of chitosan in sample **CHT$_{2.5\%}$**, namely, the aliphatic CHs in the range of 2950 cm^{-1}, around 1560 cm^{-1} it is possible to observe a vibration band representing the NH group [30], around 1300 cm^{-1} the vibration band represents the CH_2 bond. When analyzing the crosslinked chitosan spectrum, a vibration at 1100 cm^{-1} is observed, representing the C-O-C from the EGDE. In Figure 15 B. When comparing the PIL spectra and the PIL Incorporated aerogel, the vibration related to the CH aromatic groups from 3000-3100 cm^{-1} and CH aliphatic groups at around 2900–3000 cm^{-1} is detected. The presence of PIL in *AEROSAILs* is observed in the vibrations around 1580cm^{-1} related to C=N bond, and also in the 1180 cm^{-1} vibrations due to the C-N bond, confirming the incorporation of PIL in the aerogel [33].

In figure 15.B, the influence of NH_2 is visible at 3300 cm^{-1} in the IL vibration band and very weak in the CHT$_{2.5\%}$:EGD$_{32\%}$:IL1$_{50\%}$, confirming a subtle incorporation of IL in the aerogel. [30].

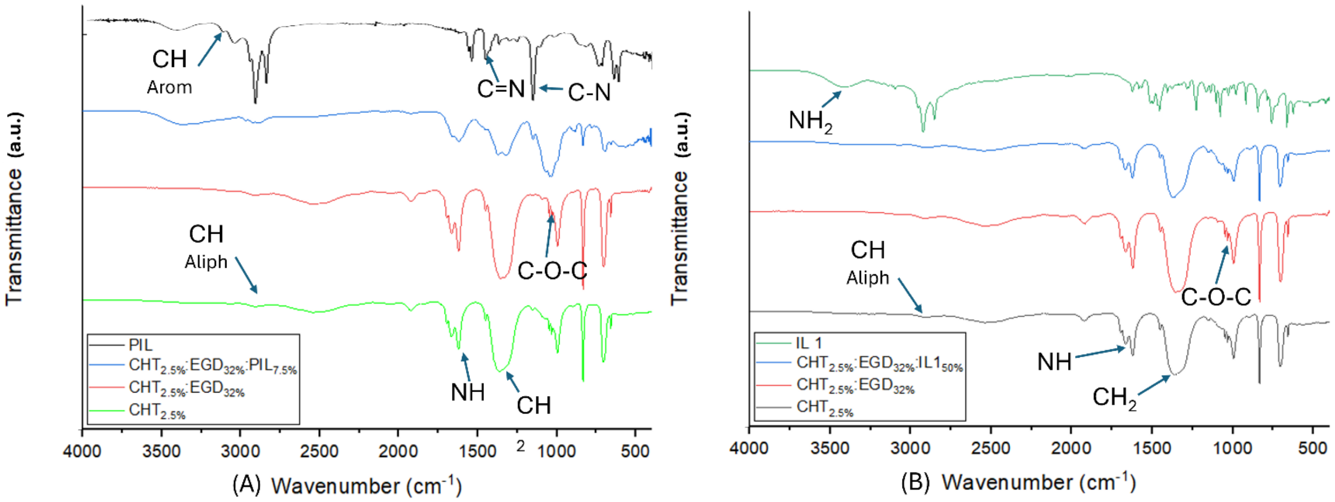

Figure 15 ATR-FTIR spectrum comparison of chitosan aerogel with EGDE and PIL (A) ; ATR-FTIR spectrum comparison of chitosan aerogel with EGDE and IL (B).

The *AEROSAILs* bead dimensions were determined using the Image J v1.53e software developed by the U.S. National Institutes of Health in Bethesda, MD, USA, which provided an analysis of the digital images of chitosan beads in hydrogel, alcogel, and aerogel states, enabling the calculation of volume shrinkage at each stage of processing based on their measured diameter and volume (Table 2). Data were derived from the examination of a minimum of approximately 20 beads. The aerogel beads' envelope density (ρ_{env}) was computed as the ratio between the average mass of particles determined through a precision balance (Model PIONEER PX 224, OHAUS, United States of America) and the dimensions extracted through image analysis.

Table 3 Influence of various components in the physicochemical properties of the aerogels.

Entry	**Particles**	**Diameter (mm)**	**ρ_{env} (g/cm^3)**	**Overall Volume Shrinkage (%)**
1	**CHT$_{2.5\%}$**	2.79	0.115	73.0
2	**CHT$_{2.5\%}$:EGD$_{32\%}$**	3.25	0.090	67.6
3	**CHT$_{2.5\%}$:EGD$_{32\%}$:T>50 °C**	2.96	0.150	79.9
4	**CHT$_{2.5\%}$:EGD$_{32\%}$:IL1$_{30\%}$**	2.92	0.080	72.4
5	**CHT$_{2.5\%}$:EGD$_{32\%}$:IL1$_{50\%}$**	2.79	0.097	71.0
6	**CHT$_{2.5\%}$:STR$_{10\%}$:EGD$_{32\%}$:IL1$_{50\%}$**	3.23	0.063	55.5
7	**CHT$_{2.5\%}$:PIL$_{15\%}$**	3.17	0.084	67.8
8	**CHT$_{2.5\%}$:EGD$_{32\%}$:PIL$_{7.5\%}$**	3.19	0.082	72.1
9	**CHT$_{2.5\%}$:PIL$_{7.5}$**	3.35	0.066	67.5
10	**CHT$_{1.5\%}$:EGD$_{32\%}$:PIL$_{50\%}$**	3.35	0.051	82.3
11	**CHT$_{2.0\%}$:EGD$_{32\%}$:PIL$_{50\%}$**	2.48	0.138	81.4
12	**CHT$_{2.5\%}$:STR$_{10\%}$:EGD$_{32\%}$:PIL$_{50\%}$**	3.44	0.061	57.8

The overall volume shrinkage of the chitosan-based aerogels varies between 55.5% and 82.3%. The samples crosslinked with PIL (**CHT$_{2.5\%}$:EGD$_{32\%}$:PIL$_{7.5\%}$**, **CHT:PIL$_{7.5}$**, **CHT$_{1.5\%}$:EGD$_{32\%}$:PIL$_{50\%}$**, **CHT$_{2.0\%}$:EGD$_{32\%}$:PIL$_{50\%}$**) generally exhibit higher shrinkage values, with (**CHT$_{1.5\%}$:EGD$_{32\%}$:PIL$_{50\%}$**) showing the highest shrinkage of 82.3%. This increase in shrinkage could be attributed to the formation of denser networks due to a higher degree of crosslinking than the samples in the presence of higher percentages of PIL. On the other hand, the samples with incorporated starch (**$CHT_{2.5\%}$:$STR_{10\%}$:$EGD_{32\%}$:$IL1_{50\%}$** and **$CHT_{2.5\%}$:$STR_{10\%}$:$EGD_{32\%}$:$PIL1_{50\%}$**) show the lowest volume shrinkage, at 55.5% and 57.8%, respectively. The starch likely acts as a reinforcing agent, contributing to a more rigid structure that resists shrinkage during drying.

The envelope density ρ_{env} (g/cm^3) of the aerogels ranges from 0.051 g/cm^3 to 0.150 g/cm^3, with the highest density observed in the sample in the entry 3, which was treated at higher temperatures (> 50 °C). This suggests that thermal treatment promotes the densification of the aerogel matrix. The presence of PIL in the samples has a noticeable effect on envelope density. The samples crosslinked with PIL, particularly entries 10 and 12, show relatively lower envelope densities (0.051-0.084 g/cm^3), indicating that while PIL may increase shrinkage, it does not contribute to an increase in envelope density. This suggests that the PIL might induce smaller pores, leading to a more compact structure. In contrast, the addition of starch (**$CHT_{2.5\%}$:$STR_{10\%}$:$EGD_{32\%}$:$IL1_{50\%}$, $CHT_{2.5\%}$:$STR_{10\%}$:$EGD_{32\%}$:$PIL1_{50\%}$**) results in lower envelope densities (0.063-0.061 g/cm^3) compared to the PIL-only samples. This suggests that starch might contribute to a more open or less compact structure, which decreases the overall density of the aerogels.

When comparing the samples containing chitosan and EGDE with similar samples where IL and PIL were incorporated, it can be concluded that the incorporation of IL leads to a reduction in the diameter (3.23mm) of the bead in entry 6 (**$CHT_{2.5\%}$:$STR_{10\%}$:$EGD_{32\%}$:$IL1_{50\%}$**). On the other hand, incorporating PIL tends to slightly increase the diameter (3.44mm) of the bead in entry 12 (**$CHT_{2.5\%}$:$STR_{10\%}$:$EGD_{32\%}$:$PIL1_{50\%}$**). In terms of envelope density, it can be observed that PIL, when incorporated, causes a decrease in the envelope density shown in entries 8 and 12 (**$CHT_{2.5\%}$:$STR_{10\%}$:$EGD_{32\%}$:$PIL1_{50\%}$, $CHT_{2.5\%}$:$EGD_{32\%}$:$PIL_{7.5\%}$**). Whereas IL (in a bigger percentage) slightly increases the envelope density , as shown in entry 6 (**$CHT_{2.5\%}$:$STR_{10\%}$:$EGD_{32\%}$:$IL1_{50\%}$**).

A comparison between the beads studied in this thesis with those previously studied by this group, more specifically in [27], was made. In the work performed during this thesis, a noticeable decrease in bead size and a significant increase in shrinkage were observed. Introducing more hydrophobic entities appears to alter the balance between hydrophilicity and hydrophobicity, leading to an apparent reduction in bead size and an increase in shrinkage.

Upon analyzing all the data, it is noticeable that the biggest changes occur during the beads' hydrogel phase (aqueous phase). The addition of PIL in the beads produced in this work contrasts with the reference articles, where the envelope density increased. In the current work, however, the envelope density decreased which may influence CO_2 capture. This suggests that the interaction between the hydrophilic and hydrophobic components during the hydrogel stage plays a key role in influencing the beads' shrinkage and final textural properties.

Building on the analysis of volume shrinkage and envelope density, it is crucial to examine how these structural changes influence the textural properties of the aerogels. Incorporating ILs, PILs, and starch affects shrinkage and density and significantly determines in determining key factors like specific surface area, pore volume, and pore diameter. Processing conditions such as temperature have a profound impact on the overall structure.

The textural properties (a_{BET}, $V_{P,BJH}$, and $D_{P,BJH}$) of PIL-chitosan aerogel particles were determined using nitrogen adsorption-desorption analysis (Table 3). The introduction of different additives and processing conditions significantly influenced these properties. For instance, the specific surface area (a_{BET})of chitosan aerogels increased markedly upon the incorporation of IL and PIL and the presence of heating (T>50 °C), particularly in the samples in entries 3 and 8, where values reached 404 m^2/g and 384 m^2/g, respectively. This enhancement is likely due to the improved porosity and network structure.

Notably, the sample (**$CHT_{2.5\%}$:$EGD_{32\%}$:T>50 °C**), which was processed at a higher temperature (T>50 °C), showed the highest specific surface area, suggesting that thermal conditions play a critical role in optimizing the textural properties. On the other hand, adding PIL at a 15% concentration (entry 7) resulted in a lower specific surface area than other samples, indicating that higher PIL concentrations may be less effective in enhancing porosity, probably due to pore blockage.

The specific pore volume ($V_{P,BJH}$) and pore diameter ($D_{P,BJH}$) also varied across the samples, with the highest specific pore volume observed (entry 3), which further supports the significant impact of processing conditions on the aerogel's textural characteristics. These findings highlight the importance of carefully tuning the composition and processing parameters to achieve the desired textural properties in chitosan-based aerogels.

To further discuss the influence of starch in the composition of the aerogel samples, we can look at entries 6 and 12, where starch was added ($STR_{10\%}$) to the formulation. Both samples show a reduction in specific surface area (a_{BET}) compared to other formulations. Entry 6 has a specific surface area of 190 m^2/g, while entry 12 has 239 m^2/g. Incorporating starch seems to result in lower surface areas, suggesting that adding starch may densify the network structure, thereby limiting porosity.

However, it's interesting to note that the pore diameter ($D_{P,BJH}$) in these samples is relatively large, especially in entry 6 (20.5 nm), which is the highest in the entire table. Entry 12, though slightly lower, still has a considerable pore diameter of 15.9 nm. This implies that while the starch might decrease the surface area, it may also contribute to forming larger pores, which could be advantageous in certain applications requiring macroporosity or controlled diffusion.

Table 4 Textural properties evaluated by nitrogen adsorption-desorption tests of *AEROSAILs.*

Entry	**Particles**	**a_{BET} (m^2/g)**	**$V_{P,BJH}$ (cm^3/g)**	**$D_{P,BJH}$ (nm)**
1	**$CHT_{2.5\%}$**	200	0.95	18.7
2	**$CHT_{2.5\%}:EGD_{32\%}$**	313	1.43	17.6
3	**$CHT_{2.5\%}:EGD_{32\%}:T>50\ °C$**	404	1.87	17.2
4	**$CHT_{2.5\%}:EGD_{32\%}:IL1_{30\%}$**	315	1.44	17.4
5	**$CHT_{2.5\%}:EGD_{32\%}:IL1_{50\%}$**	312	1.49	18.2
6	**$CHT_{2.5\%}:STR_{10\%}:EGD_{32\%}:IL1_{50\%}$**	190	0.99	20.5
7	**$CHT_{2.5\%}:PIL_{15\%}$**	234	1.09	18.1
8	**$CHT_{2.5\%}:EGD_{32\%}:PIL_{7.5\%}$**	384	1.67	16.5
9	**$CHT_{2.5\%}:PIL_{7.5}$**	366	1.59	16.7
10	**$CHT_{1.5\%}:EGD_{32\%}:PIL_{50\%}$**	205	0.94	17.5
11	**$CHT_{2.0\%}:EGD_{32\%}:PIL_{50\%}$**	262	1.15	14.9
12	**$CHT_{2.5\%}:STR_{10\%}:EGD_{32\%}:PIL1_{50\%}$**	239	1.13	15.9

Figure 14 presents two selected samples' nitrogen adsorption/desorption isotherms (**$CHT_{2.5\%}:EGD_{32\%}:PIL_{7.5\%}$).** Since the behavior of the remaining aerogels is quite similar, we can draw similar conclusions. (Please see the isotherms related to the remaining samples in the appendix. pág. 50)

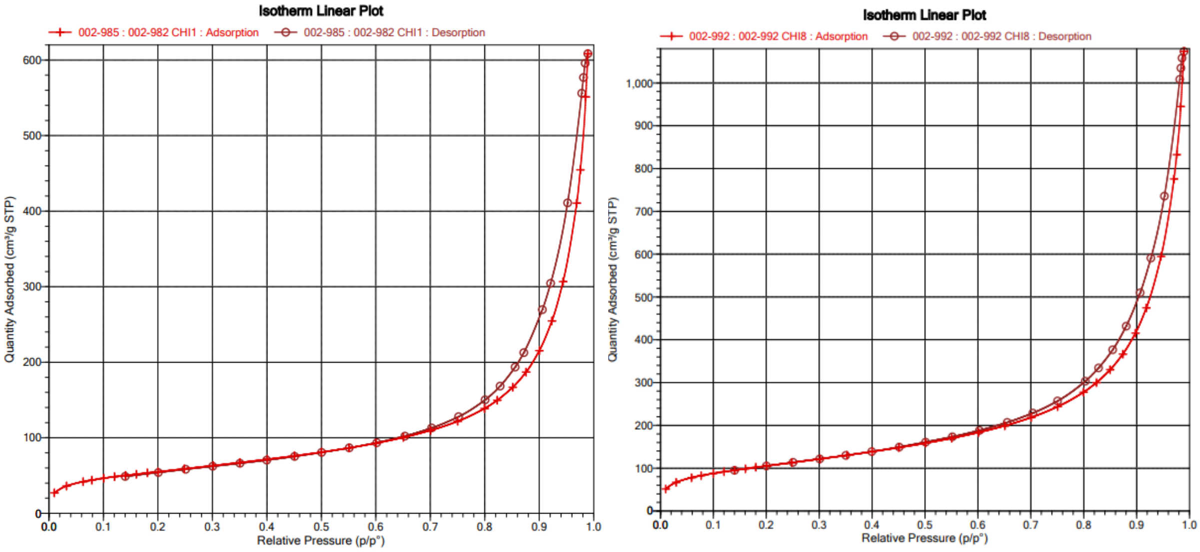

Figure 16 N_2 adsorption/desorption isotherm at 77 K of samples **CHT$_{2.5\%}$** and **CHT$_{2.5\%}$:EGD$_{32\%}$:PIL$_{7.5\%}$**.

In these isotherms, the adsorption curve gradually increases the amount of N_2 adsorbed as the relative pressure (P/P_0) increases. Below P/P_0=0.1, the amount of N_2 adsorbed rises slowly, suggesting that the initial adsorption occurs in the material's smaller pores. From P/P_0=0.5, the curve begins to incline more steeply, indicating that multilayer adsorption or the filling of larger pores starts to occur. The desorption curve closely follows the adsorption curve, again suggesting no significant hysteresis. The absence of hysteresis indicates that the material has accessible pores, and that the adsorption/desorption process is reversible [34].

These graphs suggest that the material is not predominantly microporous but likely contains mesopores. The curve resembles a Type IV isotherm, where slow adsorption occurs at low pressures, and a rapid increase in adsorption happens at higher relative pressures ($P/P_0 > 0.9$), suggesting mesopore filling. The characteristic shape of a Type IV curve includes a sharper rise at higher relative pressures due to capillary condensation in larger pores. These conclusions are similar to those previously presented in *AEROPILs* [20].

Some of the most promising beads with higher specific surface areas were further analyzed using SEM imaging. Figure 17 presents SEM micro-images of the obtained chitosan aerogels in several relevant compositions. For comparison, SEM images of chitosan beads with the same amount of IL, but one with and another without the crosslinker, are also shown (c, d for the surface and g, h for the interior). The particles' inner and outer regions show the dual porous structure. The crosslinker's presence leads to the formation of more organized fibers, with a corresponding reduction in pore diameter. Moreover, the integration of PIL alters the fiber structure, as it seems to envelop them (Figures 17 d and h). It becomes clear that both the PIL alone and the PIL combined with the crosslinker result in notable alterations in fiber architecture and arrangement, as also validated by SEM images.

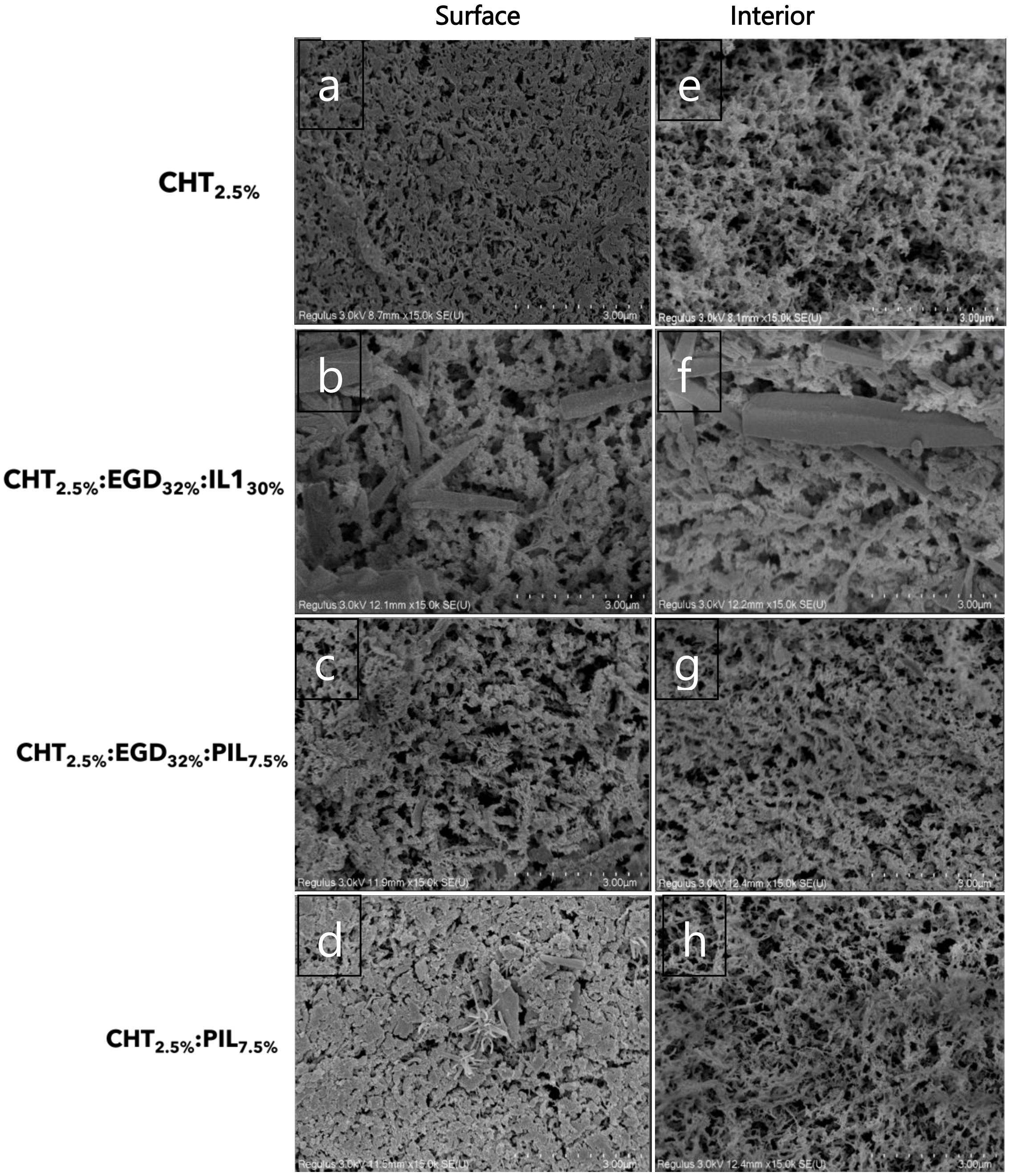

Figure 17 Textural appearance of CHT; $CHT_{2.5\%}:EGD_{32\%}:IL1_{30\%}$; $CHT_{2.5\%}:EGD_{32\%}:PIL_{7.5\%}$; $CHT_{2.5\%}:PIL_{7.5\%}$) beads at the surface (a,b,c,d), respectively; and in the interior (e,f,g,h) respectively.

3.3 Catalytic activity of *AEROSAILs*

A comprehensive screening process was conducted through batch reactions to pinpoint the most efficient catalysts and refine their future application in continuous flow systems for industrial use. The catalysts chosen for this study were evaluated based on their structural and textural characteristics, effectiveness in promoting the reaction, and performance across various conditions. The outcomes of these reactions were determined by analyzing the conversion and selectivity percentages through ^{1}H NMR analysis according to the appendix on pág. 52, as summarized in Table 5, alongside the reaction times; the catalytic mechanism that was proposed by Barrulas *et al.* [27] for *AEROPILs* can be envisioned for *AEROSAILs* as well, being represented in Figure 18.

During the catalysis process, the epoxide (butylene oxide (BTO) or epichlorohydrin (ECH)) reacts with CO_2 for 24 to 72 hours under a pressure of 10 bar and at 135 °C. The reaction product is later dissolved in deuterated chloroform to proceed with ^{1}H NMR analysis to assess each aerogel's conversion efficiency and selectivity.

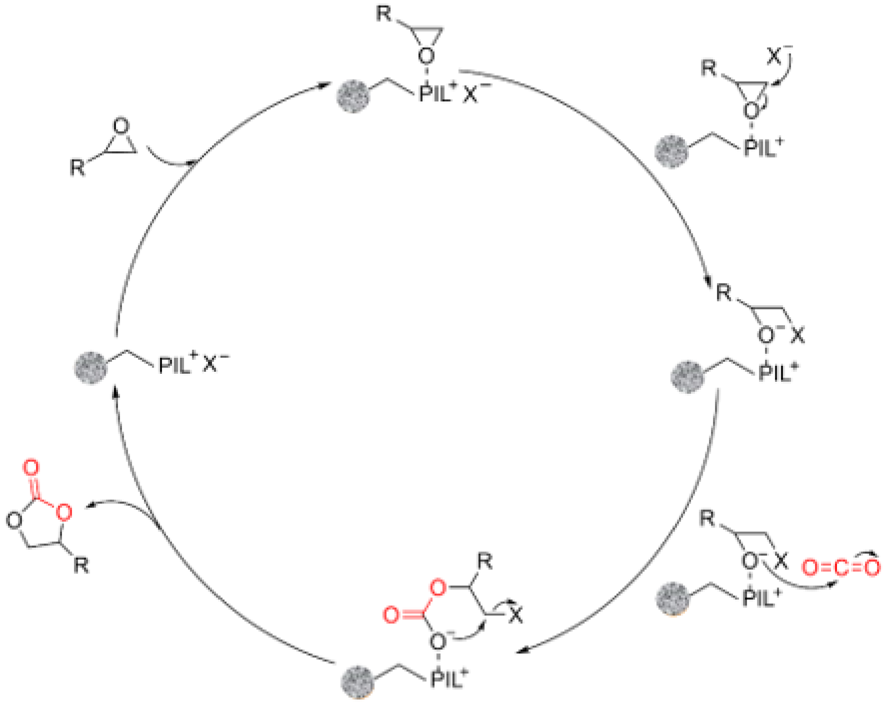

Figure 18 Proposed catalytic mechanism for the CO2 fixation with epoxides promoted by hydrogen-bond donors and Cl- or Br- anions in the AEROPIL catalyst (the interac tion between the AEROPIL and the substrate is represented with dashed lines) [27].

Table 5 Batch CO_2 cycloaddition catalysed by *AEROSAILs*.

Entry	Catalyst	Pre-treatment	Time (h)	Conversion (%)	Selectivity (%)	Epoxide
1	**CHT$_{2.5\%}$:EGD$_{32\%}$:PIL$_{7.5\%}$**	NO	24	2	99	BTO
2	**CHT$_{2.5\%}$:EGD$_{32\%}$:IL1$_{50\%}$**	NO	24	4	60	BTO
3	**CHT$_{2.5\%}$:PIL$_{7.5}$**	NO	72	14	56	BTO
4	**CHT$_{2.5\%}$:EGD$_{32\%}$**	NO	24	2	34	BTO
5	**IL 1**	NO	24	99	99	BTO
6	**CHT$_{2.5\%}$:PIL$_{15\%}$**	YES	72	29	76	BTO
7	**CHT$_{2.5\%}$:EGD$_{32\%}$:PIL$_{7.5\%}$**	YES	72	42	59	BTO
8	**CHT$_{2.0\%}$:EGD$_{32\%}$:PIL$_{50\%}$**	YES	72	32	91	BTO
9	**CHT$_{2.5\%}$:STR$_{10\%}$:EGD$_{32\%}$:PIL1$_{50\%}$**	YES	72	46	70	BTO
10	**CHT$_{2.5\%}$:STR$_{10\%}$:EGD$_{32\%}$:IL1$_{50\%}$**	YES	72	8	77	BTO
11	**CHT$_{2.5\%}$:STR$_{10\%}$:EGD$_{32\%}$:PIL1$_{50\%}$**	YES	72	71	92	ECH

The introduction of pre-treatment (PRE) significantly enhances the catalytic activity compared to the untreated catalysts containing PIL. The pre-treatment enhances the catalytic efficiency and improves the desired product's selectivity. Untreated catalysts without any IL or PIL, like **CHT$_{2.5\%}$:EGD$_{32\%}$** (entry 4), showed minimal conversion (2%) and lower selectivity (34%) after 24 hours, underscoring the importance of this procedure for the activity of the IL-based systems [27].

Attempts to improve selectivity and conversion were made by altering the catalyst composition and reaction conditions. For example, using a higher amount of PIL and EGDE as a crosslinker when compared to other samples, as in **CHT$_{2.0\%}$:EGD$_{32\%}$:PIL$_{50\%}$** (entry 8), results in a more favorable balance between conversion (32%) and selectivity (91%) when compared to entry 6. Notably, experiments using starch as a component of the catalyst show promising results in PIL-based *AEROSAILs* (entries 9 and 11). Entry 11 (**CHT$_{2.5\%}$:STR$_{10\%}$:EGD$_{32\%}$:PIL1$_{50\%}$**) with a starch-containing catalyst and a high PIL loading achieved a conversion of 71% when using epichlorohydrin as epoxide **(E)**, with a selectivity of 92%, indicating significant progress towards optimizing both parameters. However, in *AEROSAILs* with IL (entries 2 and 10), despite the high conversion and selectivity achieved with the pristine IL (entry 5), the respective inclusion in the aerogel cannot successfully catalyze the desired reaction. In this case, even with the pre-treatment, no significant improvement was observed (entries 2 and 10).

The overall selectivity for PIL based *AEROSAILs* in these conditions remains moderate to high, indicating that the reaction conditions are favorable for producing the cyclic carbonate. It is worth mentioning that these reactions were carried out under conditions of temperature and pressure intended to resemble those of exhaust gases on industrial chimneys, emphasizing these systems' potential environmental and economic benefits.

The beads that exhibited the highest performance in terms of selectivity and conversion **($CHT_{2.5\%}$:$STR_{10\%}$:$EGD_{32\%}$:$PIL1_{50\%}$)** were then tested for five catalytic cycles using butylene oxide **(B)** as an epoxide proving its capability to be reused. The performance of the beads during 5 cycles is shown in Figure 19.

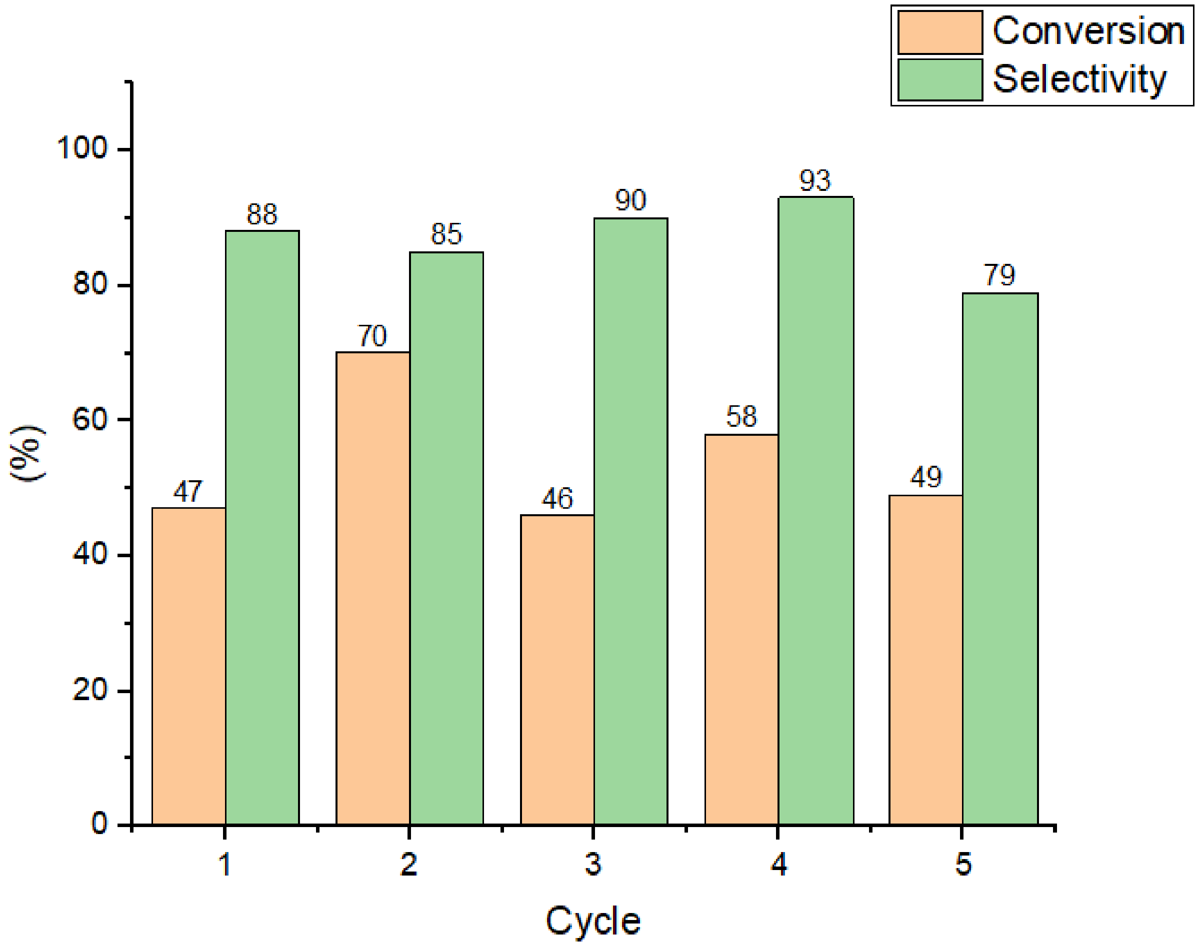

Figure 19 CO_2 cycloaddition catalysed by *AEROSAIL* **$CHT_{2.5\%}$:$STR_{10\%}$:$EGD_{32\%}$:$PIL_{50\%}$** without co-catalyst and solvent with subsequent regeneration.

As shown in Figure 19, the aerogel beads demonstrated effective reusability, maintaining a relatively high conversion rate with some variability. The conversion rate ranged from a minimum of 46% to a maximum of 71%. The ability to reuse the aerogels is crucial for the sustainability of this project, especially for industrial applications where reusable materials are essential to justify future scaling up. Notably, the second cycle exhibited the highest conversion rate, which could be attributed to several factors.

Firstly, the washing treatment after the first cycle may have more effectively removed residual impurities or structural water from deeper within the aerogel increasing the conversion rate when compared to the samples previously studied in this thesis, thereby exposing more active catalytic sites in the second cycle and enhancing the interaction between the epoxide and the aerogel. Secondly, there is a possibility that the cyclic carbonate formed during the first catalytic reaction remained trapped within the *AEROSAIL* structure and was not fully expelled during washing with diethyl ether. This hypothesis, however, requires further investigation to be confirmed.

When comparing these results from recycling experiments with previous ones obtained in the research group and in the same conditions described in *AEROPILS* [27], the conversion rates are less constant (variation of 24%) and slightly lower, however the selectivity is comparable. In the former work, the *AEROPILs* contained 80% PIL, nevertheless, in the currents study the *AEROSAILs* contain 50% PIL. This difference could signify that the use of surface-active PILs can be beneficial for CO_2 cycloaddition catalysis.

4

CONCLUSION AND FUTURE PERSPECTIVES

This dissertation successfully demonstrated the synthesis and characterization of chitosan-based aerogels enhanced with ionic liquids (ILs) and poly(ionic liquids) (PILs) with surface active properties - *AEROSAILs*. Incorporating these components significantly improved the aerogels' structural integrity and textural properties, as evidenced by comprehensive characterization techniques, including ATR-FTIR, NMR, and nitrogen adsorption-desorption analysis. The resulting aerogels exhibited remarkable surface areas, reaching up to 404 m^2/g, highlighting their potential for various applications in fields such as catalysis and environmental remediation. The morphological evaluation via SEM revealed distinct changes in the aerogel architecture, emphasizing the role of PILs in modulating fiber structures.

The catalytic performance assessments illustrated the effective activity of these aerogels in carbon dioxide (CO_2) cycloaddition reactions, achieving conversion rates of up to 71%. The aerogel reuse demonstrated consistent catalytic performance, with the second cycle achieving the highest conversion rate, followed by slight variations in subsequent cycles as the material gradually stabilized and retained its efficiency over time. These findings underscore the significance of tailored chitosan-based aerogels as multifunctional materials.

While this study provides significant insights into the properties and applications of chitosan-based aerogels, several avenues for future research remain. One critical area is the scalability and production of these aerogels. Investigating scalable production methods will be crucial for practical applications, necessitating research into batch processing techniques and optimizing synthesis parameters to enhance the feasibility of large-scale manufacturing.

Furthermore, future studies could explore the functionalization of aerogels with additional bioactive compounds or nanoparticles to further enhance their properties, such as antibacterial activity or specific catalytic capabilities. This would broaden the application spectrum and optimize performance in targeted environments.

The potential of chitosan-based aerogels in environmental applications, particularly in water purification and CO_2 capture, also warrants further exploration. Assessing their performance in real-world conditions and investigating their long-term stability is vital to ensure practical implementation. Developing aerogels that can effectively remove pollutants from water or capture greenhouse gases could significantly contribute to environmental sustainability.

Addressing these future research directions will fully realize the potential of chitosan-based aerogels, leading to innovative applications and contributing to the sustainable development of advanced materials. The continuous evolution of this field promises exciting opportunities for interdisciplinary collaboration, ultimately advancing material science and its practical applications in society.

REFERENCES

[1] W. Silva, M. Zanatta, A. S. Ferreira, M. C. Corvo, and E. J. Cabrita, "Revisiting ionic liquid structure-property relationship: A critical analysis," Oct. 02, 2020, *MDPI AG*. doi: 10.3390/ijms21207745.

[2] M. Wang, L. Zhang, L. Gao, K. Pi, J. Zhang, and C. Zheng, "Improvement of the CO2 absorption performance using ionic liquid [NH2emim][BF4] and [emim][BF4]/[bmim][BF 4] mixtures," *Energy and Fuels*, vol. 27, no. 1, pp. 461–466, Jan. 2013, doi: 10.1021/ef301541s.

[3] H. Kumar and G. Kaur, "Scrutinizing Self-Assembly, Surface Activity and Aggregation Behavior of Mixtures of Imidazolium Based Ionic Liquids and Surfactants: A Comprehensive Review," May 13, 2021, *Frontiers Media S.A.* doi: 10.3389/fchem.2021.667941.

[4] M. Stanton Ribeiro, M. Zanatta, and M. C. Corvo, "Ionic liquids and biomass as carbon precursors: Synergistically answering a call for CO2 capture and conversion," Nov. 01, 2022, *Elsevier Ltd*. doi: 10.1016/j.fuel.2022.125164.

[5] J. Yuan, D. Mecerreyes, and M. Antonietti, "Poly(ionic liquid)s: An update," 2013, *Elsevier Ltd*. doi: 10.1016/j.progpolymsci.2013.04.002.

[6] W. Qian, J. Texter, and F. Yan, "Frontiers in poly(ionic liquid)s: Syntheses and applications," Feb. 21, 2017, *Royal Society of Chemistry*. doi: 10.1039/c6cs00620e.

[7] R. V. Barrulas, M. Zanatta, T. Casimiro, and M. C. Corvo, "Advanced porous materials from poly(ionic liquid)s: Challenges, applications and opportunities," May 01, 2021, *Elsevier B.V.* doi: 10.1016/j.cej.2021.128528.

[8] A. S. Shaplov, D. O. Ponkratov, and Y. S. Vygodskii, "Poly(ionic liquid)s: Synthesis, properties, and application," Mar. 01, 2016, *Maik Nauka-Interperiodica Publishing*. doi: 10.1134/S156009041602007X.

[9] M. Hasib-ur-Rahman, M. Siaj, and F. Larachi, “Ionic liquids for CO2 capture-Development and progress,” Apr. 2010. doi: 10.1016/j.cep.2010.03.008.

[10] K. E. Gutowski and E. J. Maginn, “Amine-functionalized task-specific ionic liquids: A mechanistic explanation for the dramatic increase in viscosity upon complexation with CO2 from molecular simulation,” *J Am Chem Soc*, vol. 130, no. 44, pp. 14690–14704, Nov. 2008, doi: 10.1021/ja804654b.

[11] M. Kharazi, J. Saien, and S. Asadabadi, “Review on Amphiphilic Ionic Liquids as New Surfactants: From Fundamentals to Applications,” Feb. 01, 2022, *Springer Science and Business Media Deutschland GmbH*. doi: 10.1007/s41061-021-00362-6.

[12] A. Kulshrestha, P. S. Gehlot, and A. Kumar, “Paramagnetic surface active ionic liquids: synthesis, properties, and applications,” Aug. 01, 2021, *Elsevier Ltd*. doi: 10.1016/j.mtchem.2021.100522.

[13] C. S. Buettner, A. Cognigni, C. Schröder, and K. Bica-Schröder, “Surface-active ionic liquids: A review,” Feb. 01, 2022, *Elsevier B.V.* doi: 10.1016/j.molliq.2021.118160.

[14] J. Yang *et al.*, “Versatile Aerogels for Sensors,” Oct. 01, 2019, *Wiley-VCH Verlag*. doi: 10.1002/smll.201902826.

[15] W. Wu, S. Dong, X. Zhang, and J. Hao, “Gel electrolytes and aerogel electrodes from ILs-based emulsions for supercapacitor applications,” *Chemical Engineering Journal*, vol. 446, Oct. 2022, doi: 10.1016/j.cej.2022.137328.

[16] T. Heinrich, U. Klety, and J. Fricke, “Aerogels Nanoporous Materials Part h Sol-Gel Process and Drying of Gels,” Kluwer Academic Publishers, 1995.

[17] H. Li, J. Li, A. Thomas, and Y. Liao, “Ultra-High Surface Area Nitrogen-Doped Carbon Aerogels Derived From a Schiff-Base Porous Organic Polymer Aerogel for CO2 Storage and Supercapacitors,” *Adv Funct Mater*, vol. 29, no. 40, Oct. 2019, doi: 10.1002/adfm.201904785.

[18] S. Zhao, W. J. Malfait, N. Guerrero-Alburquerque, M. M. Koebel, and G. Nyström, “Biopolymer-Aerogele und -Schäume: Chemie, Eigenschaften und Anwendungen,” *Angewandte Chemie*, vol. 130, no. 26, pp. 7704–7733, Jun. 2018, doi: 10.1002/ange.201709014.

[19] J. Fricke and T. Tillotson, “Aerogels: production, characterization, and applications,” 1997.

[20] R. V. Barrulas *et al.*, “The AEROPILs generation: Novel poly(ionic liquid)-based aerogels for CO2 capture,” *Int J Mol Sci*, vol. 23, no. 1, Jan. 2022, doi: 10.3390/ijms23010200.

[21] H. Maleki, “Recent advances in aerogels for environmental remediation applications: A review,” Sep. 15, 2016, *Elsevier B.V.* doi: 10.1016/j.cej.2016.04.098.

[22] P. C. Vilella, J. A. Lira, D. C. S. Azevedo, M. Bastos-Neto, and R. Stefanutti, "Preparation of biomass-based activated carbons and their evaluation for biogas upgrading purposes," *Ind Crops Prod*, vol. 109, pp. 134–140, Dec. 2017, doi: 10.1016/j.indcrop.2017.08.017.

[23] M. V. Gil, N. Álvarez-Gutiérrez, M. Martínez, F. Rubiera, C. Pevida, and A. Morán, "Carbon adsorbents for CO2 capture from bio-hydrogen and biogas streams: Breakthrough adsorption study," *Chemical Engineering Journal*, vol. 269, pp. 148–158, Jun. 2015, doi: 10.1016/j.cej.2015.01.100.

[24] F. Yang *et al.*, "Synthesis of Porous Carbons with High N-Content from Shrimp Shells for Efficient CO2-Capture and Gas Separation," *ACS Sustain Chem Eng*, vol. 6, no. 11, pp. 15550–15559, Nov. 2018, doi: 10.1021/acssuschemeng.8b03995.

[25] W. Wang, S. Gong, J. Liu, Y. Ge, J. Wang, and X. Lv, "Ag-Cu aerogel for electrochemical CO2 conversion to CO," *J Colloid Interface Sci*, vol. 595, pp. 159–167, Aug. 2021, doi: 10.1016/j.jcis.2021.03.120.

[26] S. Gong *et al.*, "Silk fibroin-derived carbon aerogels embedded with copper nanoparticles for efficient electrocatalytic CO2-to-CO conversion," *J Colloid Interface Sci*, vol. 600, pp. 412–420, Oct. 2021, doi: 10.1016/j.jcis.2021.05.054.

[27] R. V. Barrulas *et al.*, "Poly(ionic liquid)-based aerogels for continuous-flow CO2 upcycling," *Journal of CO2 Utilization*, vol. 83, May 2024, doi: 10.1016/j.jcou.2024.102771.

[28] X. Pan *et al.*, "Poly(ionic liquid) nanovesicles via polymerization induced self-assembly and their stabilization of Cu nanoparticles for tailored CO2 electroreduction," *J Colloid Interface Sci*, vol. 637, pp. 408–420, May 2023, doi: 10.1016/j.jcis.2023.01.097.

[29] C. López-Iglesias *et al.*, "Vancomycin-loaded chitosan aerogel particles for chronic wound applications," *Carbohydr Polym*, vol. 204, pp. 223–231, Jan. 2019, doi: 10.1016/j.carbpol.2018.10.012.

[30] A. Pawlak and M. Mucha, "Thermogravimetric and FTIR studies of chitosan blends," 2003.

[31] M. R. Kasaai, "Determination of the degree of N-acetylation for chitin and chitosan by various NMR spectroscopy techniques: A review," Mar. 17, 2010. doi: 10.1016/j.carbpol.2009.10.051.

[32] W. M. Facchinatto *et al.*, "Evaluation of chitosan crystallinity: A high-resolution solid-state NMR spectroscopy approach," *Carbohydr Polym*, vol. 250, Dec. 2020, doi: 10.1016/j.carbpol.2020.116891.

[33] W. quan Feng, Y. heng Lu, Y. Chen, Y. wei Lu, and T. Yang, “Thermal stability of imidazolium-based ionic liquids investigated by TG and FTIR techniques,” *J Therm Anal Calorim*, vol. 125, no. 1, pp. 143–154, Jul. 2016, doi: 10.1007/s10973-016-5267-3.

[34] J. Jeromenok and J. Weber, “Restricted access: On the nature of adsorption/desorption hysteresis in amorphous, microporous polymeric materials,” *Langmuir*, vol. 29, no. 42, pp. 12982–12989, Oct. 2013, doi: 10.1021/la402630s.

A

APPENDIX

A.1 Materials

In this work the following materials were used: Chitosan (deacetylation degree 75–85%, viscosity 20–300 mPa.s, Mw 50–190 kDa), 1-(3-aminopropyl)imidazole (≥ 97% purity), 1-bromodecane (98% purity), 1-vinylimidazole (≥ 99% purity) and diethyl ether (> 99.8% purity) were supplied by Sigma-Aldrich (St. Louis, MO, USA). Starch was supplied by Pan-reac AppliChem (Darmstadt, Germany). Water was purified using reverse osmosis (resistivi-ty > 18 MΩ.cm, Milli-Q, Millipore®, Madrid, Spain. Acetic acid (≥ 99.8% purity) and etha-nol (EtOH) were acquired from Honeywell (Seelze, Germany). NaOH (98% purity) was pur-chased from EKA (Bohus, Sweden). Carbon dioxide (99.98% purity) used in supercritical drying was supplied by Air Liquide (Lisboa, Portugal). Carbon dioxide (99.998% purity) supplied by Air Liquide was used in the catalytic reactions. Ethylene glycol diglycidyl ether mixture (EGDE) (SG=1.19) and 1,2-butylene oxide (99% purity) were acquired from TCI Chemicals (Tokyo, JP). DMSO-d6 (>99.80% purity) and $CDCl_3$ (> 99% purity) were supplied by Eurisotop (St-Aubin, France). Dialysis membrane 12-14kd was purchased from Spec-tra/Por (Waltham, Massachusetts, USA). Epichlorohydrin (≥99 % purity) were supplied by Sigma-Aldrich (St. Louis, MO, USA).

A.2 Characterizations

A.2.1 Brunauer–Emmett–Teller (BET)

The textural properties of the aerogel beads were evaluated using nitrogen adsorption-desorption analysis (ASAP 2000, Micromeritics, Norcross, GA, USA). Prior to analysis, the samples were degassed at 60 °C, and the measurements were conducted at 77 K. The specific surface area (a_{BET}) was determined using the Brunauer−Emmett−Teller (BET) method, while the pore size distribution was assessed via the Barrett-Joyner-Halenda (BJH) method.

A.2.2 Attenuated Total Reflectance - Fourier Transform Infrared Spectroscopy (ATR-FTIR)

ATR-FTIR spectra were acquired using a PerkinElmer Spectrum Two (Waltham, MA, USA), capturing 8 scans over the 4000 to 400 cm^{-1} range. The resulting spectra were processed using SpectraGryph 1.2.15 software.

A.2.3 Scanning Electron Microscopy (SEM)

SEM images of the aerogel beads were captured using a Hitachi Regulus 8220 Scanning Electron Microscope (Mito, Japan) equipped with energy-dispersive X-ray spectroscopy (EDS) from Oxford Instruments. Prior to imaging, the aerogel beads were sputter-coated with a 15 nm layer of iridium (Q150 T S/E/ES, Quorum Technologies, Lewes, UK) to enhance contrast.

A.2.4 Nuclear Magnetic Resonance (NMR)

The solid-state ^{13}C MAS NMR spectra were obtained using an AVANCE III Bruker spectrometer with a magnetic field strength of 11.7 T (500 MHz) and a ^{13}C operating frequency of 125 MHz. A BBO probe head was employed for the measurements, with the samples spun at the magic angle at 5 kHz in 4 mm rotors at ambient temperature. The ^{13}C MAS NMR experiments utilized proton cross-polarization, with a contact time of 2.0 ms and a recycle delay of 5.0 s. Liquid-state NMR were conducted at 298.2 K on a Bruker Avance III 400 spectrometer, set to 400.15 MHz for ^{1}H nuclei and 100.61 MHz for ^{13}C, using either a Bruker High-Resolution BBO probe equipped with a temperature control module and a gradient unit capable of generating magnetic field gradients of 50.0 G/cm along the z-axis or a water-cooled diffusion probe Bruker DiffBB driven by a 60 A gradient amplifier (GREAT60) capable of a maximum gradient along the z-axis of 1768 G/cm. Bruker Topspin 4.3.0 software was used for data acquisition and processing.

A.3 NMR SPECTRA

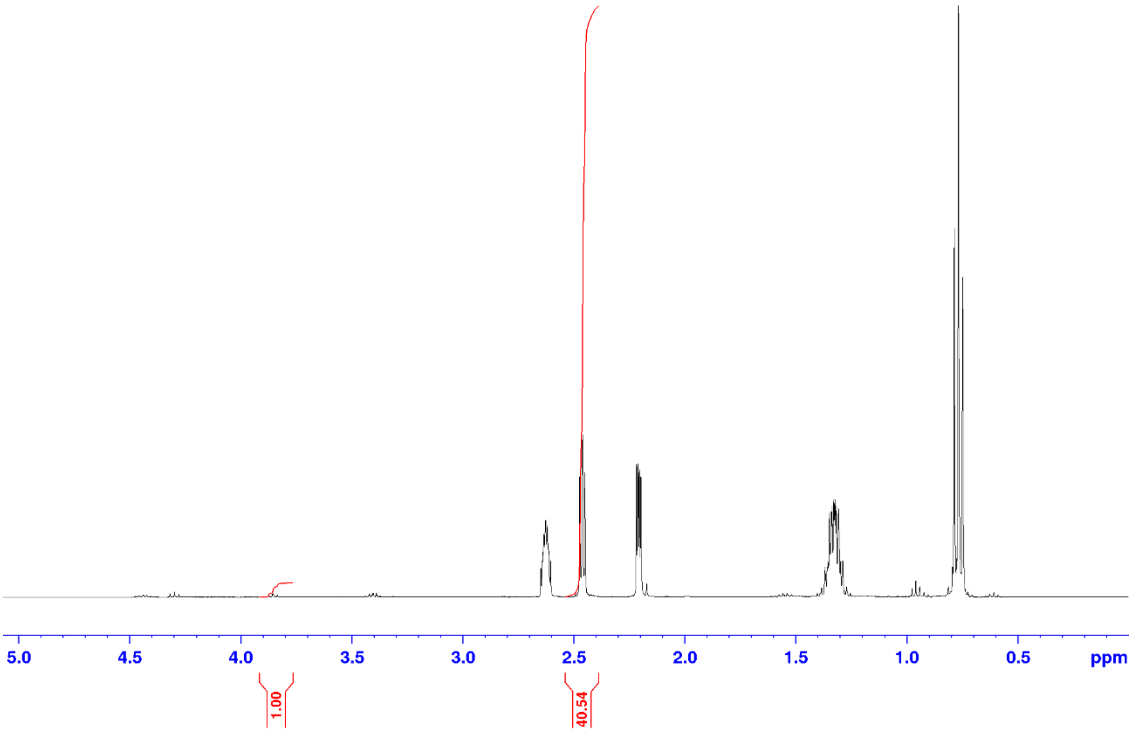

Figure 20 ^{1}H NMR spectrum of the catalysis reaction of **CHT$_{2.5\%}$:EGD$_{32\%}$:PIL$_{7.5\%}$** with butylene oxide In CDCl$_3$.

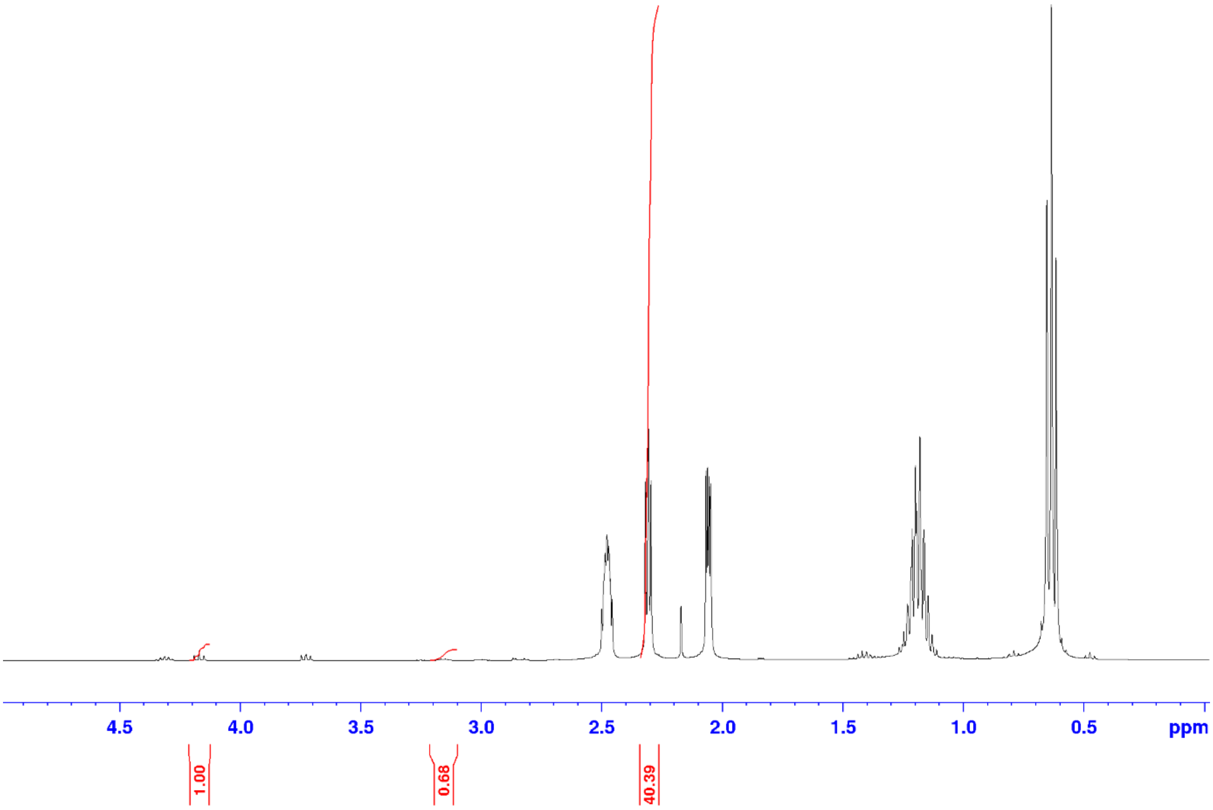

Figure 21 ^{1}H NMR spectrum of the catalysis reaction of **CHT$_{2.5\%}$:EGD$_{32\%}$:IL1$_{50\%}$**with butylene oxide In $CDCl_3$.

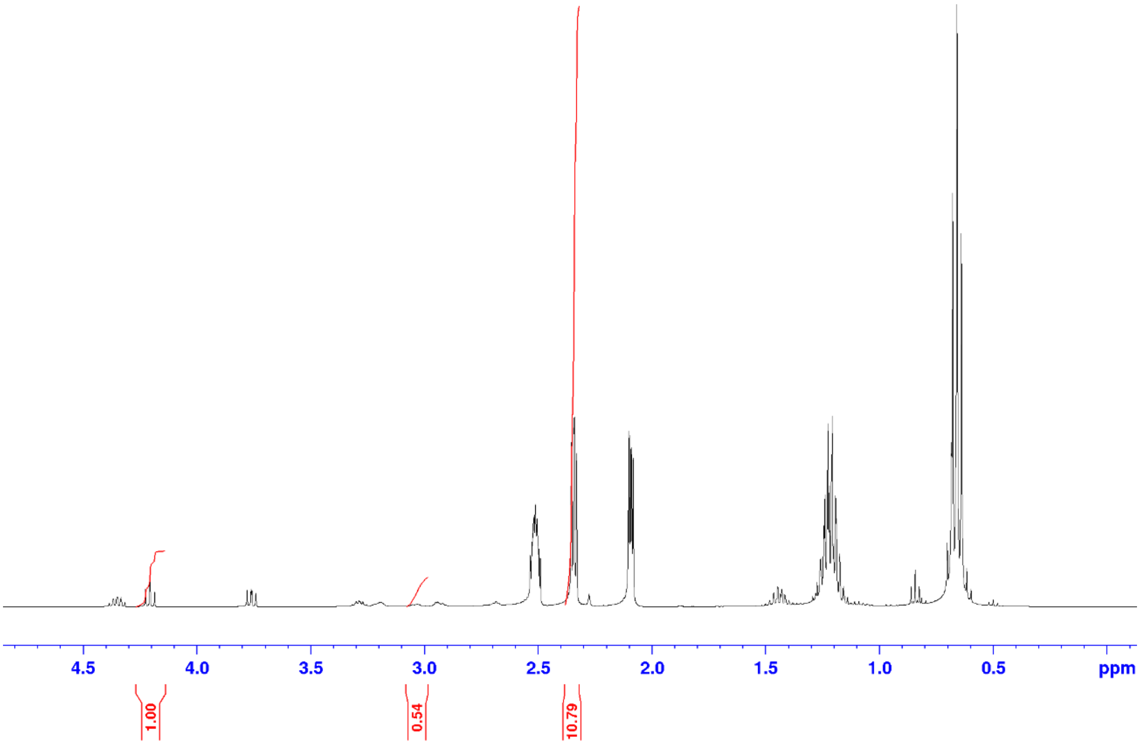

Figure 22 ^{1}H NMR spectrum of the catalysis reaction of **CHT$_{2.5\%}$:PIL$_{7.5}$**with butylene oxide In $CDCl_3$.

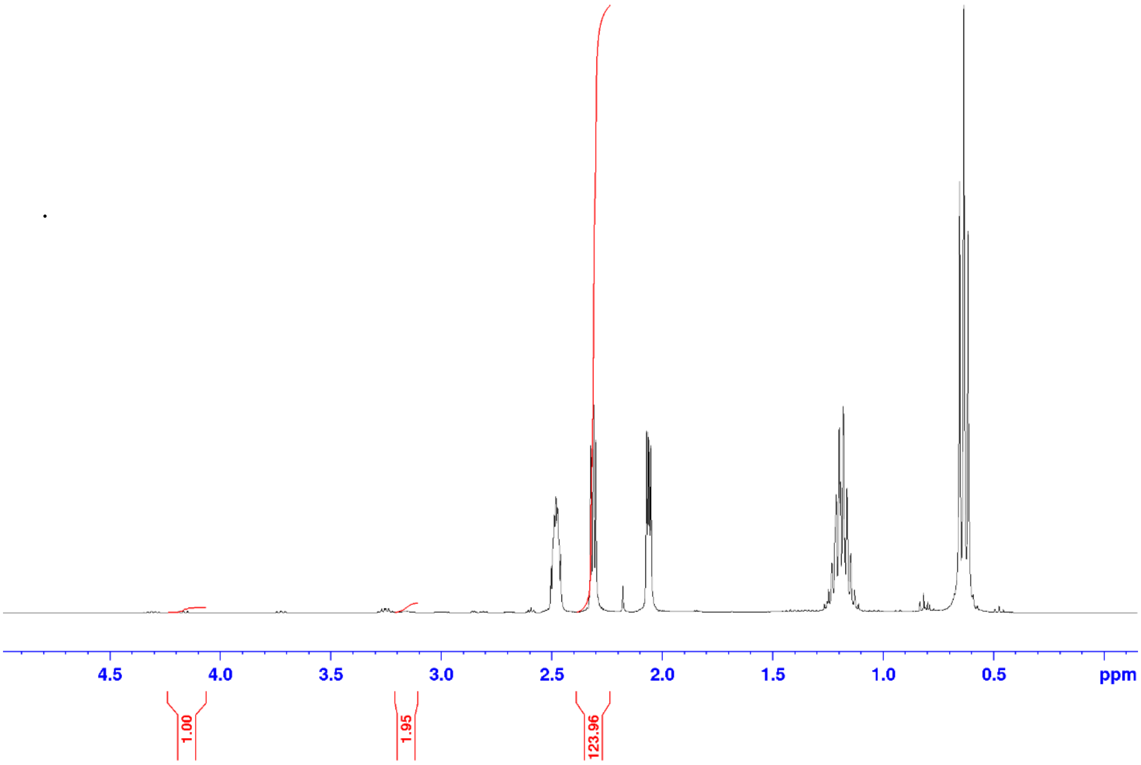

Figure 23 ^{1}H NMR spectrum of the catalysis reaction of **CHT$_{2.5\%}$:EGD$_{32\%}$**with butylene oxide In $CDCl_3$.

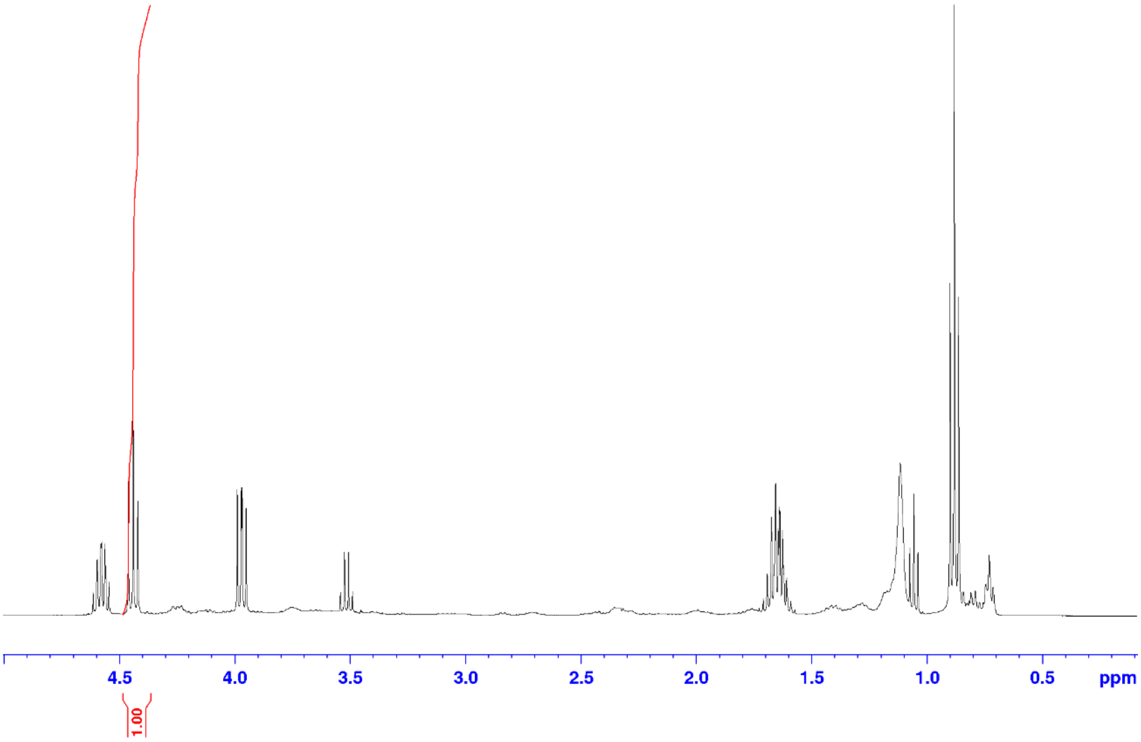

Figure 24 ^{1}H NMR spectrum of the catalysis reaction of **IL 1** with butylene oxide In $CDCl_3$.

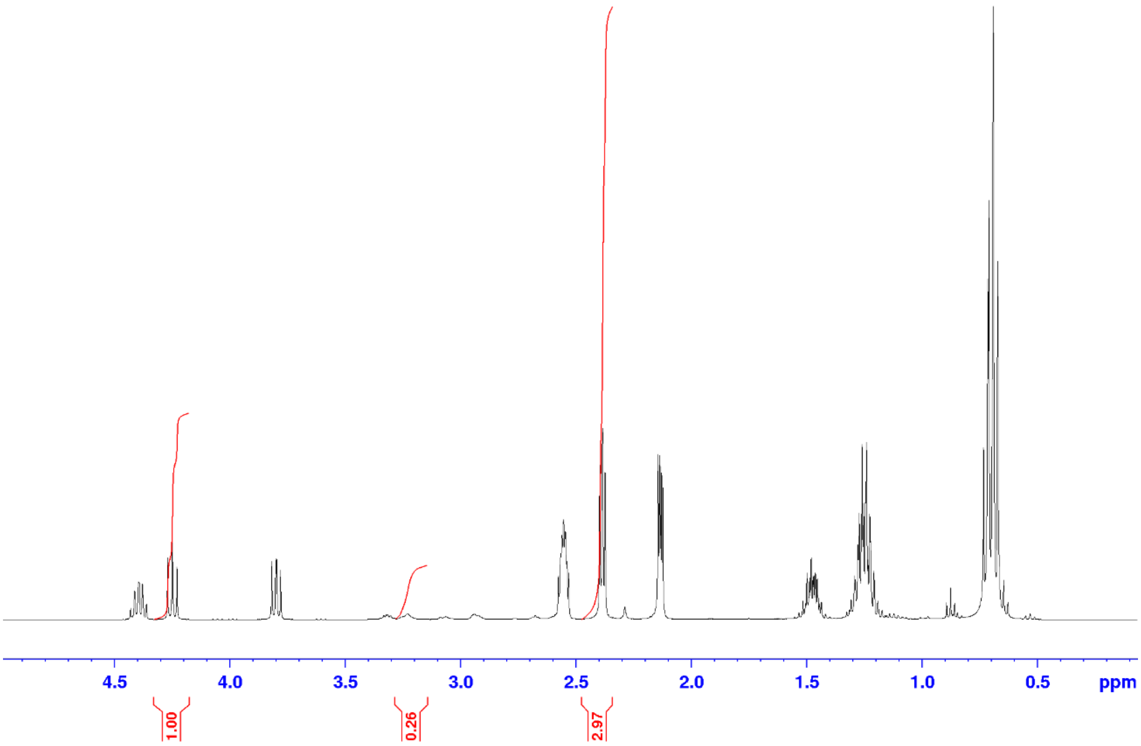

Figure 25 ^{1}H NMR spectrum of the catalysis reaction of **CHT$_{2.5\%}$:PIL$_{15\%}$**with butylene oxide In CDCl$_3$.

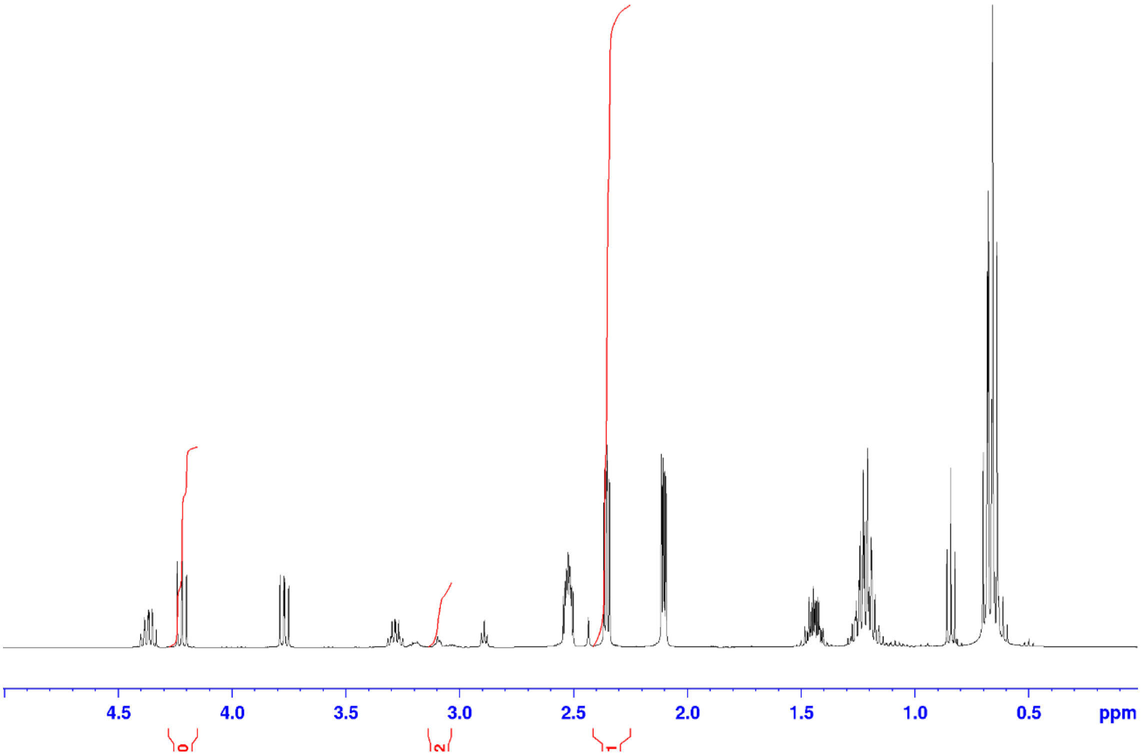

Figure 26 ^{1}H NMR spectrum of the catalysis reaction of **CHT$_{2.5\%}$:EGD$_{32\%}$:PIL$_{7.5\%\%}$** with butylene oxide In CDCl$_3$.

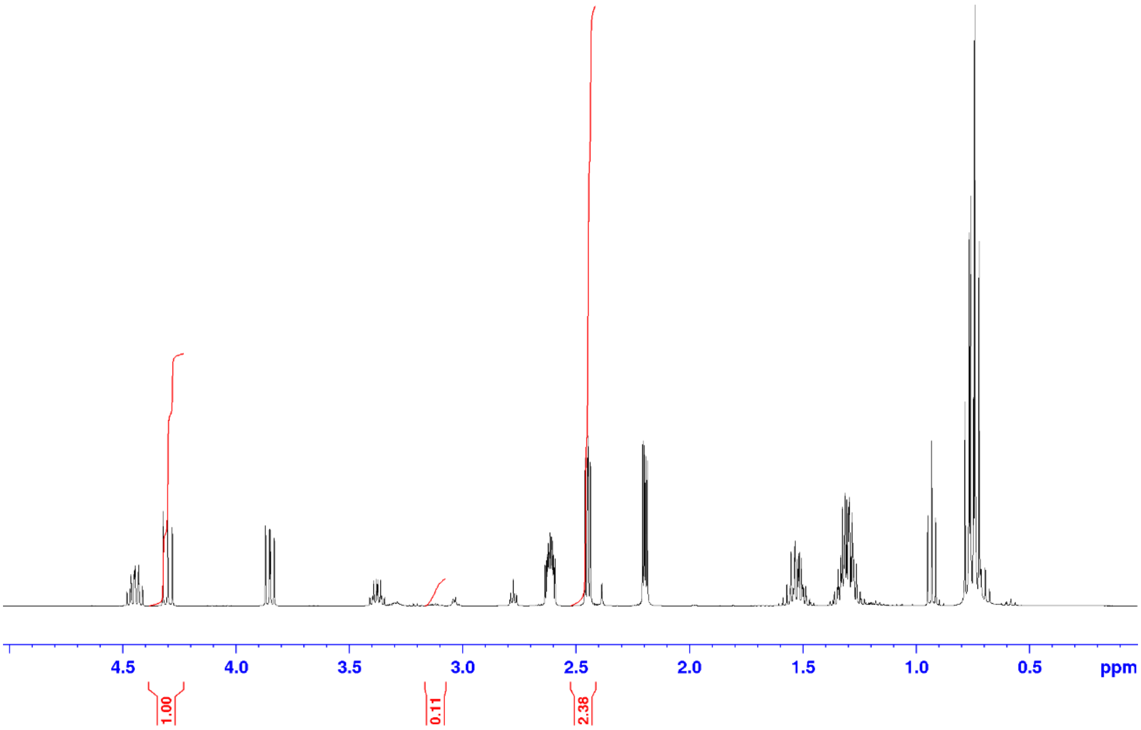

Figure 27 ^{1}H NMR spectrum of the catalysis reaction of **$CHT_{2.0\%}$:$EGD_{32\%}$:$PIL_{50\%}$**with butylene oxide In $CDCl_3$.

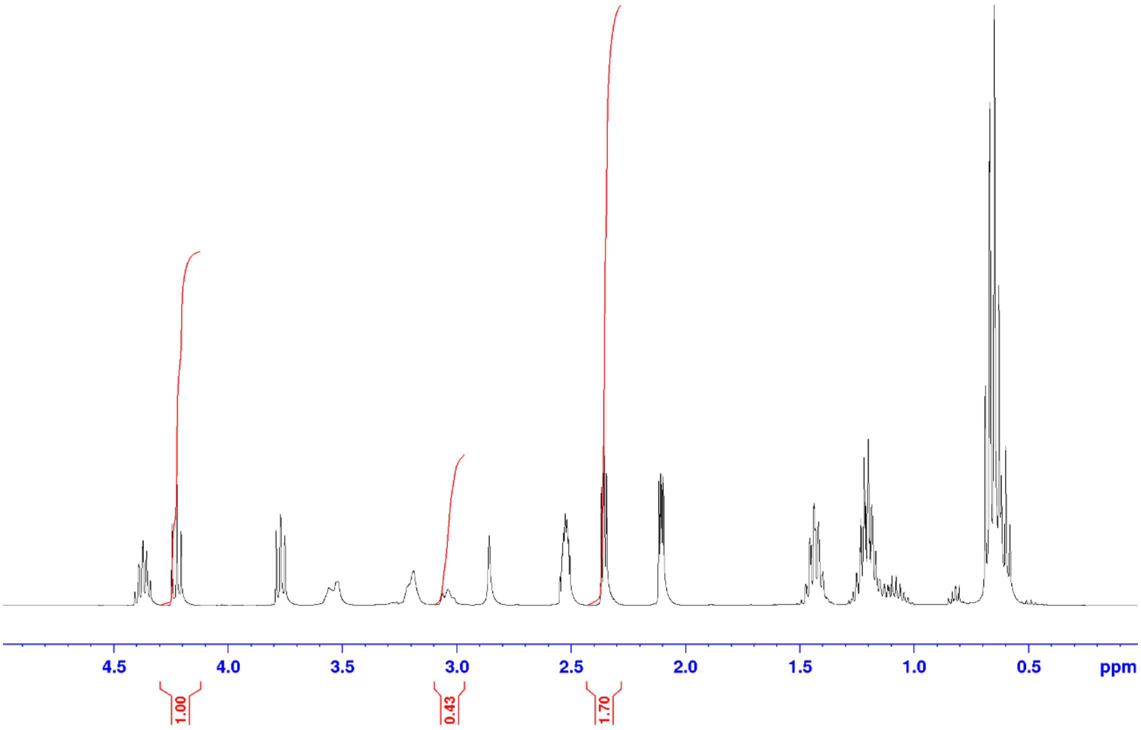

Figure 28 ^{1}H NMR spectrum of the catalysis reaction of **$CHT_{2.5\%}$:$STR_{10\%}$:$EGD_{32\%}$:$PIL1_{50\%}$**with butylene oxide In $CDCl_3$.

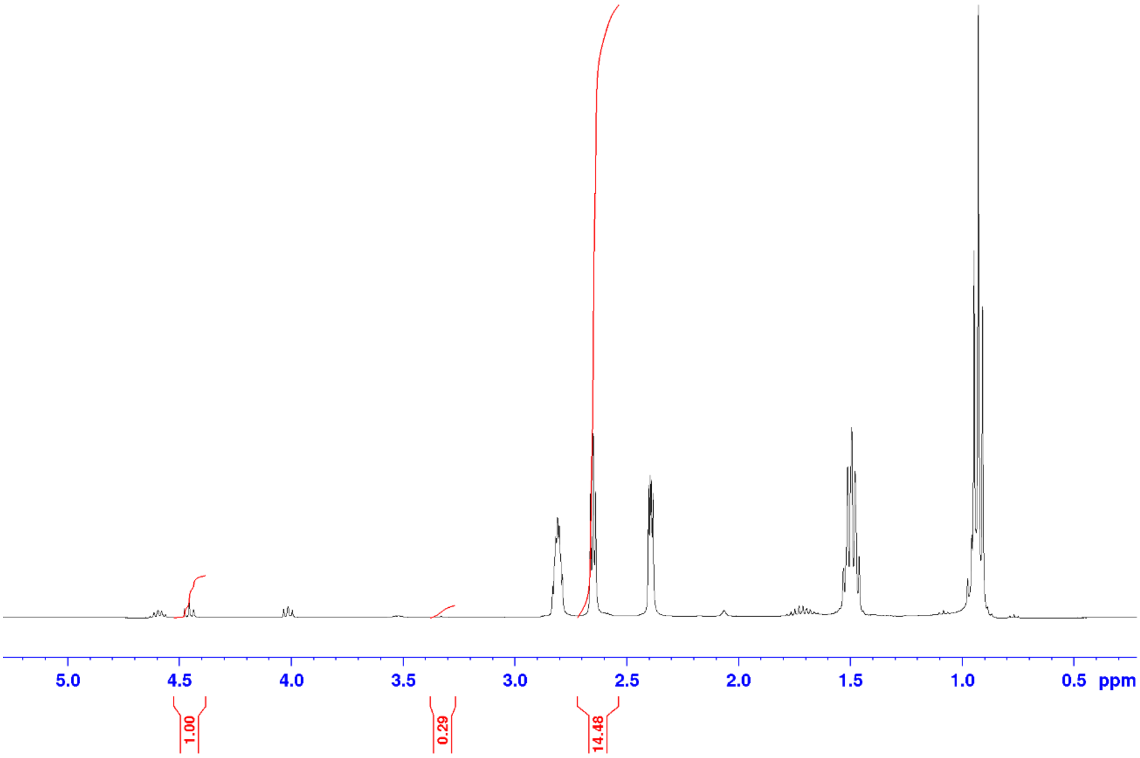

Figure 29 ^{1}H NMR spectrum of the catalysis reaction of **CHT$_{2.5\%}$:STR$_{10\%}$:EGD$_{32\%}$:IL1$_{50\%}$**with butylene oxide In CDCl$_3$.

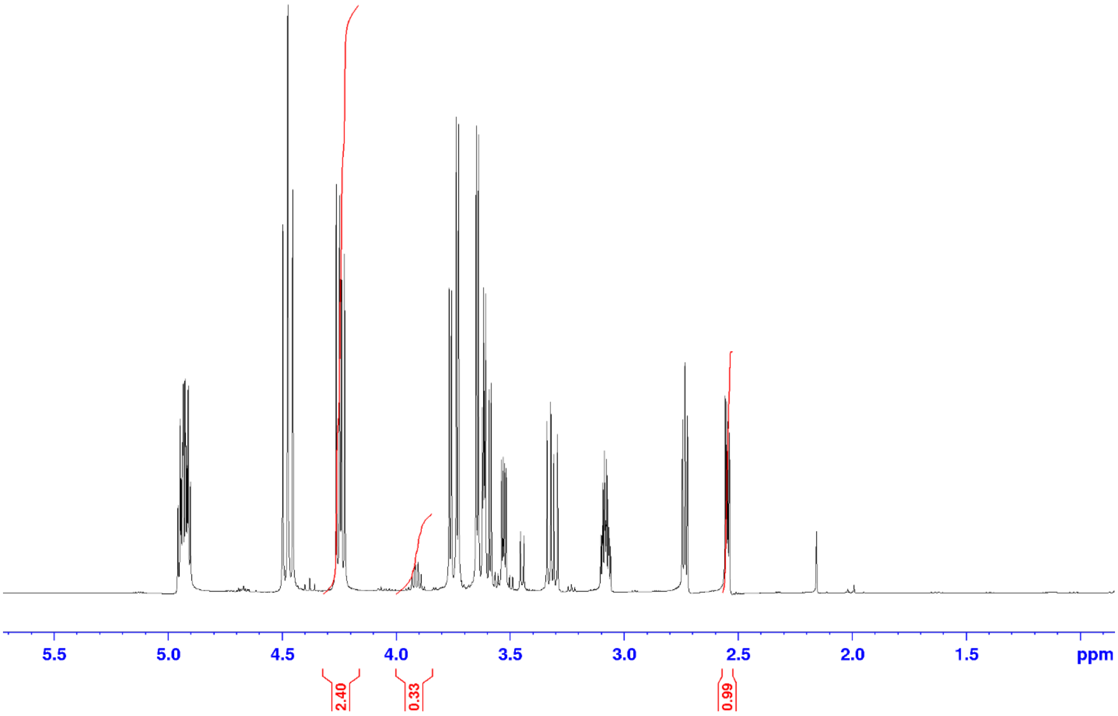

Figure 30 ^{1}H NMR spectrum of the catalysis reaction of **CHT$_{2.5\%}$:STR$_{10\%}$:EGD$_{32\%}$:PIL1$_{50\%}$**with Epichlorohydrin In CDCl$_3$.

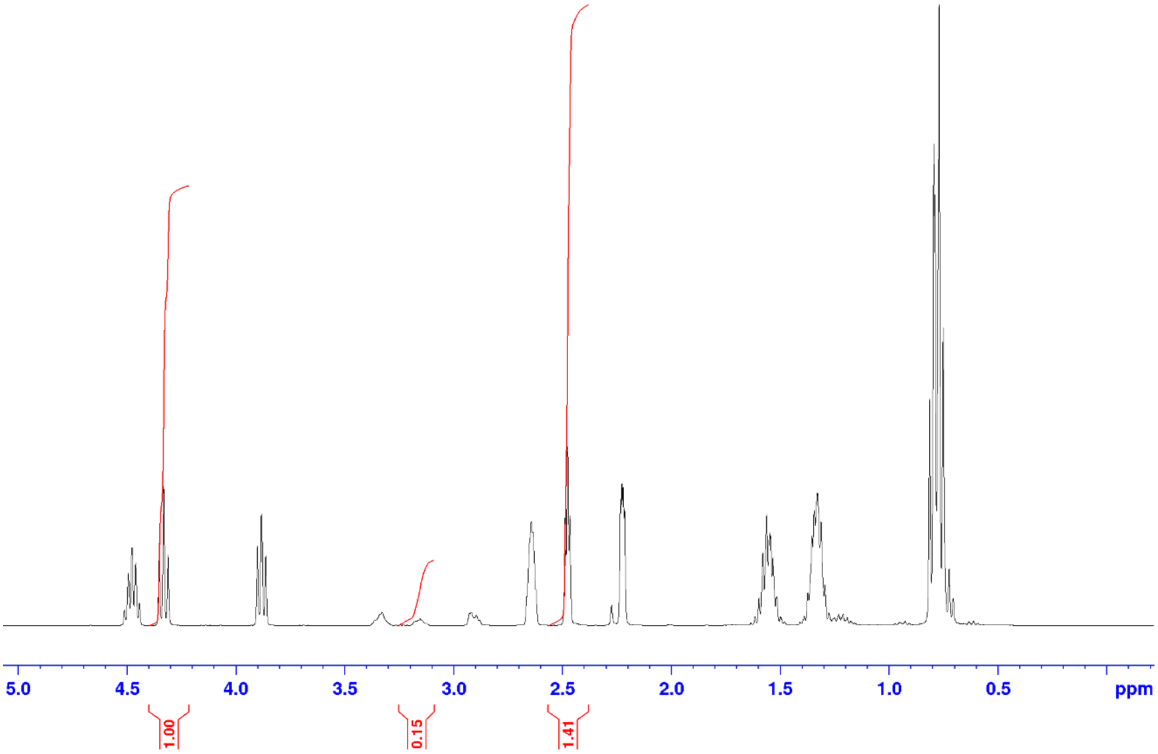

Figure 31 ^{1}H NMR spectrum of the 1st cycle catalysis reaction of **CHT$_{2.5\%}$:STR$_{10\%}$:EGD$_{32\%}$:PIL1$_{50\%}$**with butylene oxide In CDCl$_3$.

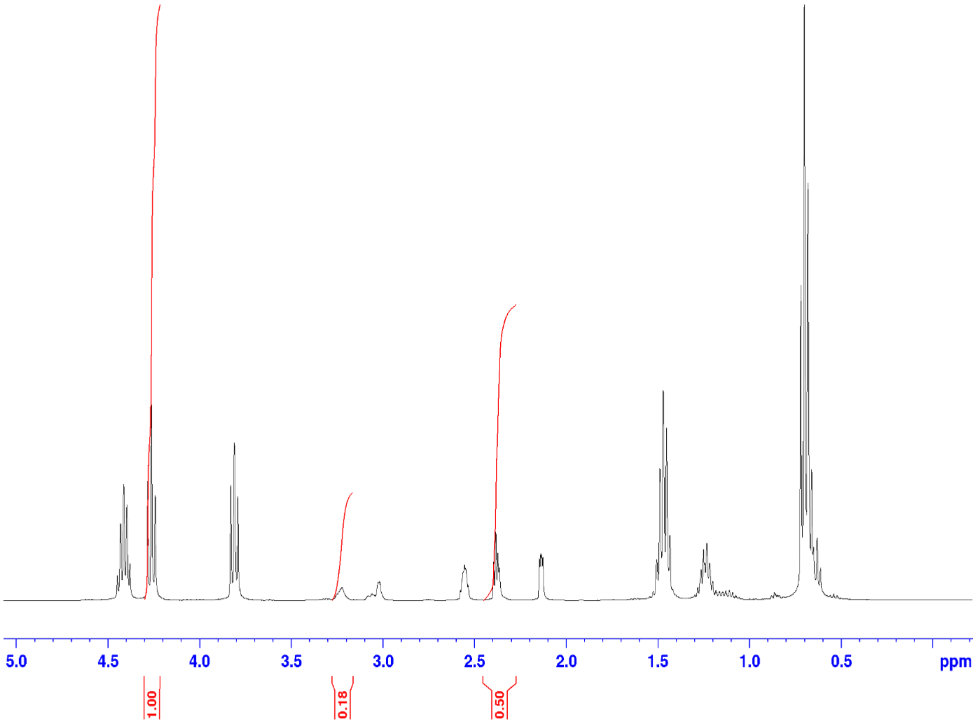

Figure 32 ^{1}H NMR spectrum of the 2nd cycle catalysis reaction of **CHT$_{2.5\%}$:STR$_{10\%}$:EGD$_{32\%}$:PIL1$_{50\%}$**with butylene oxide In CDCl$_3$.

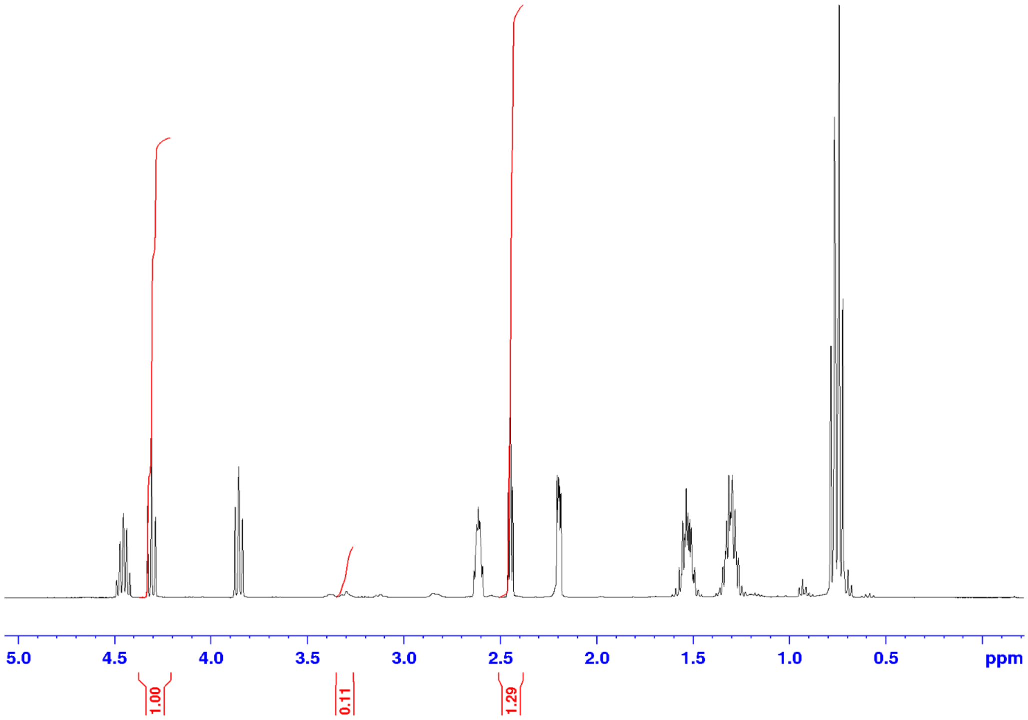

Figure 33 ^{1}H NMR spectrum of the 3rd cycle catalysis reaction of **CHT$_{2.5\%}$:STR$_{10\%}$:EGD$_{32\%}$:PIL1$_{50\%}$**with butylene oxide In CDCl$_3$.

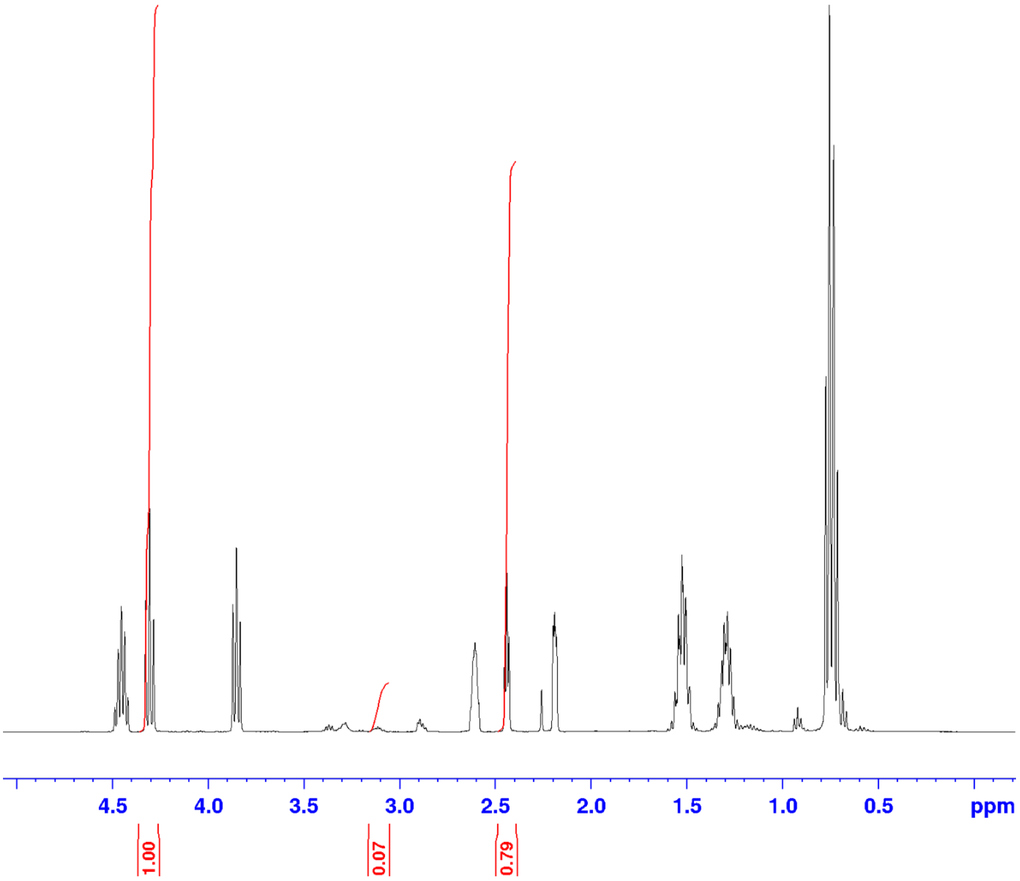

Figure 34 ^{1}H NMR spectrum of the 4th cycle catalysis reaction of **CHT$_{2.5\%}$:STR$_{10\%}$:EGD$_{32\%}$:PIL1$_{50\%}$**with butylene oxide In CDCl$_3$.

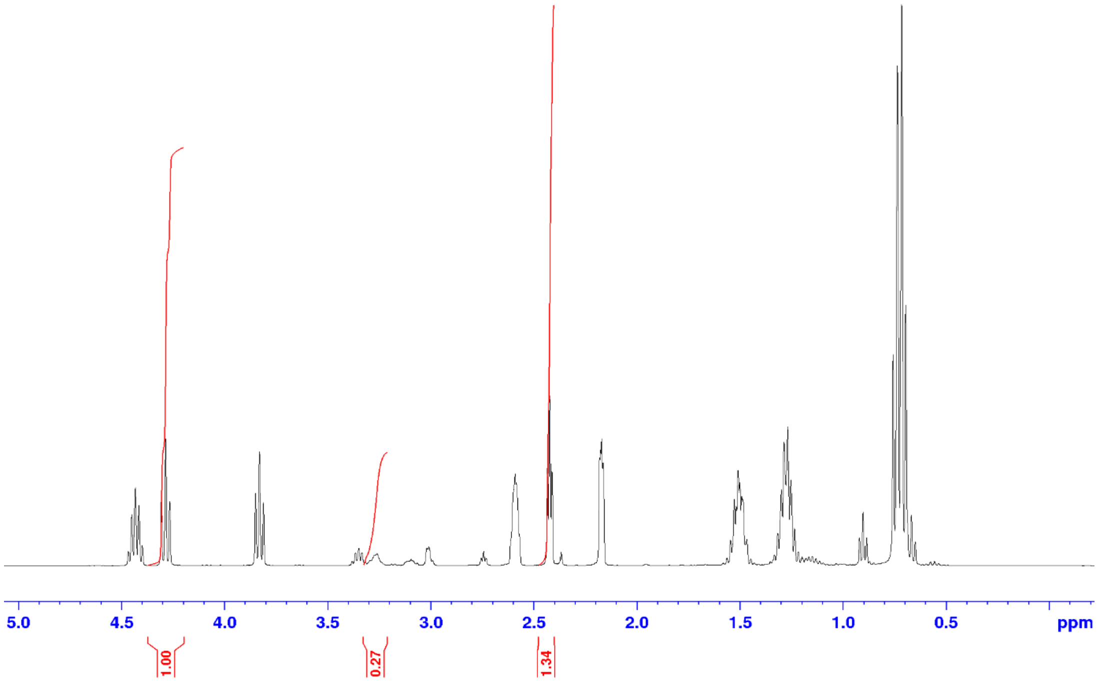

Figure 35 ^{1}H NMR spectrum of the 5th cycle catalysis reaction of **CHT$_{2.5\%}$:STR$_{10\%}$:EGD$_{32\%}$:PIL1$_{50\%}$**with butylene oxide in CDCl$_3$.

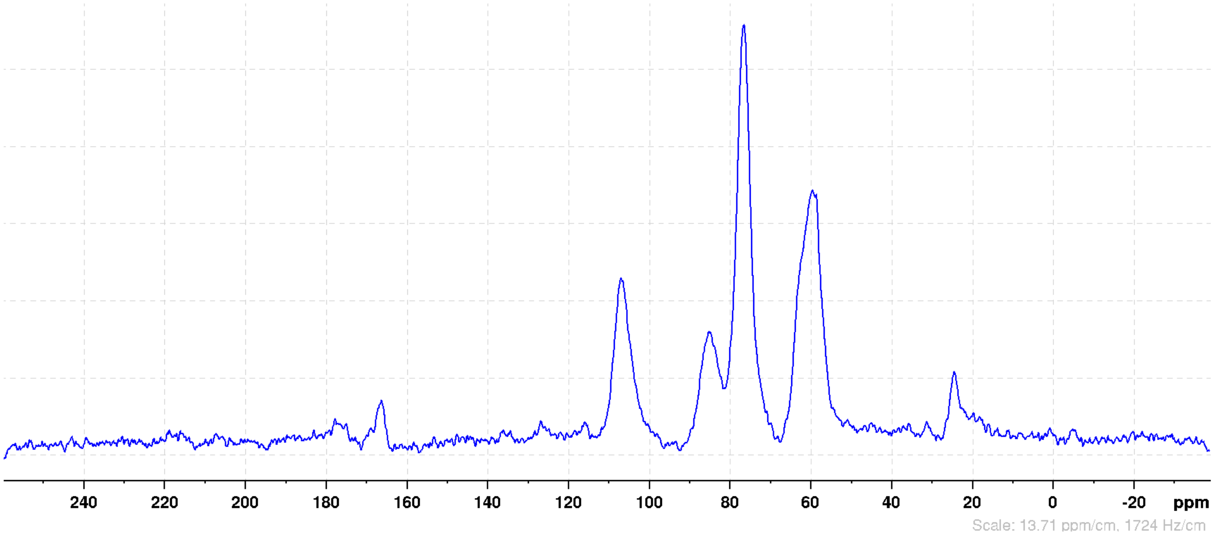

Figure 36 ^{13}C-CP TOSS NMR spectrum of **CHT$_{2.5\%}$:EGD$_{32\%}$:PIL$_{7.5\%}$.**

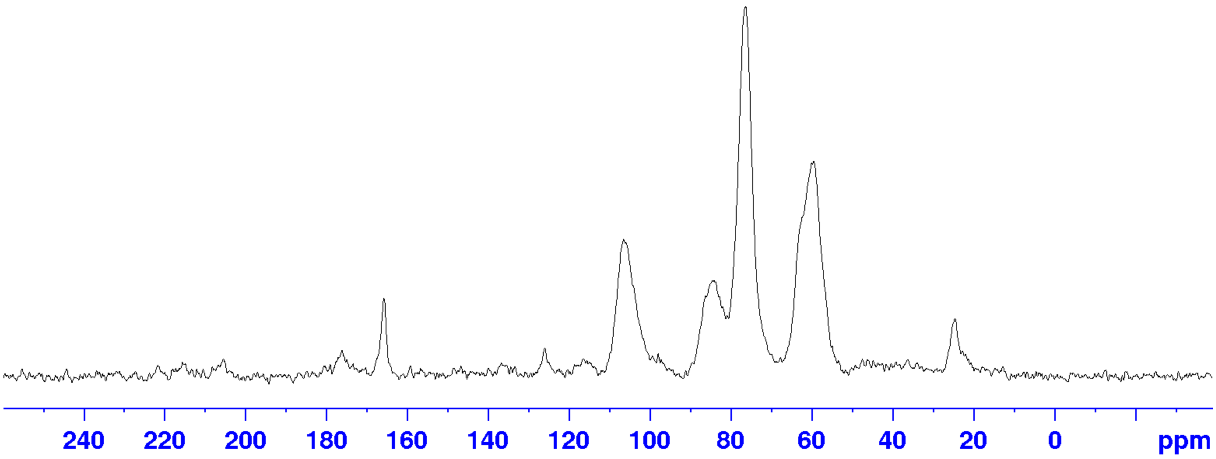

Figure 37 ^{13}C-CP TOSS NMR spectrum of **CHT$_{2.5\%}$:EGD$_{32\%}$:IL1$_{50\%}$.**

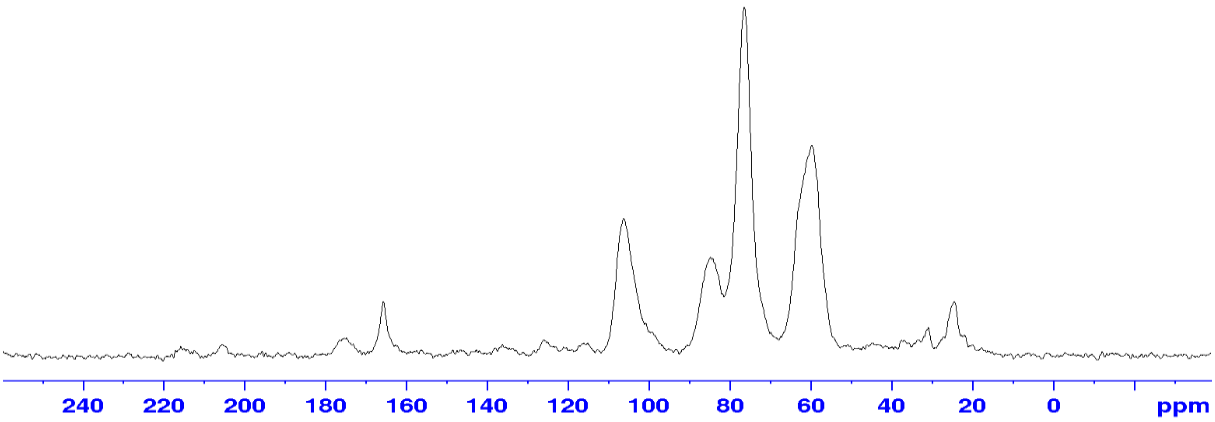

Figure 38 ^{13}C-CP TOSS NMR spectrum of **CHT$_{2.5\%}$:PIL$_{7.5}$.**

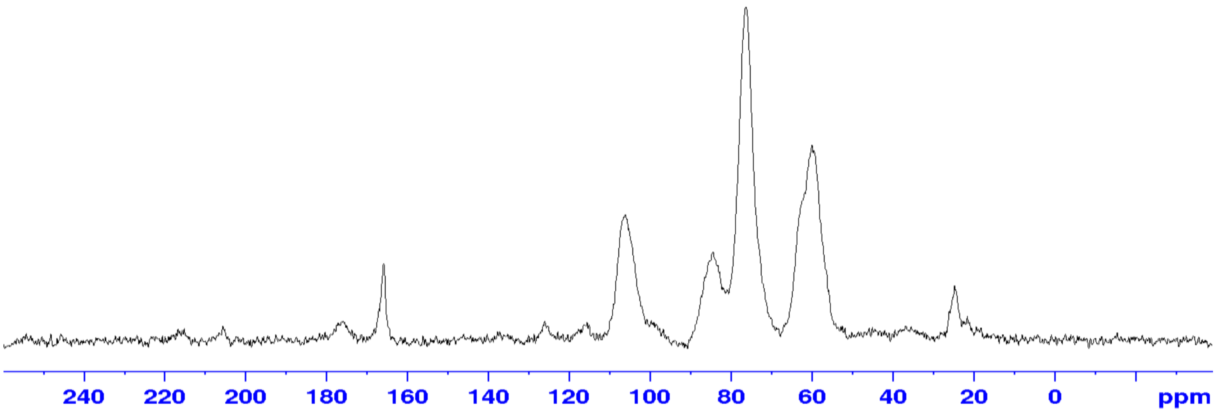

Figure 39 ^{13}C-CP TOSS NMR spectrum of **CHT$_{2.5\%}$:STR$_{10\%}$:EGD$_{32\%}$:IL1$_{50\%}$.**

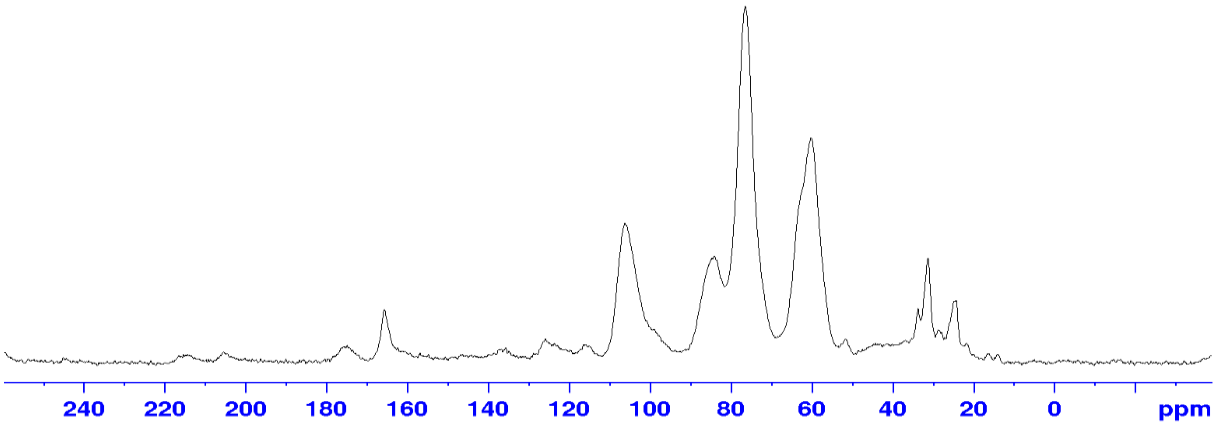

Figure 40 ^{13}C-CP TOSS NMR spectrum of **$CHT_{2.5\%}$:$STR_{10\%}$:$EGD_{32\%}$:$PIL_{50\%}$.**

A.4 BET Analysis

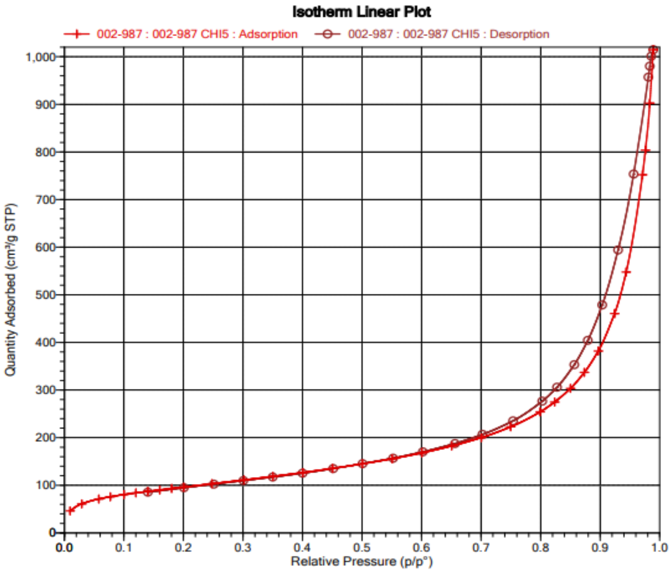

Figure 42 N$_2$ adsorption/desorption isotherm at 77 K of samples **CHT$_{2.5\%}$:EGD$_{32\%}$:T>50 ºC.**

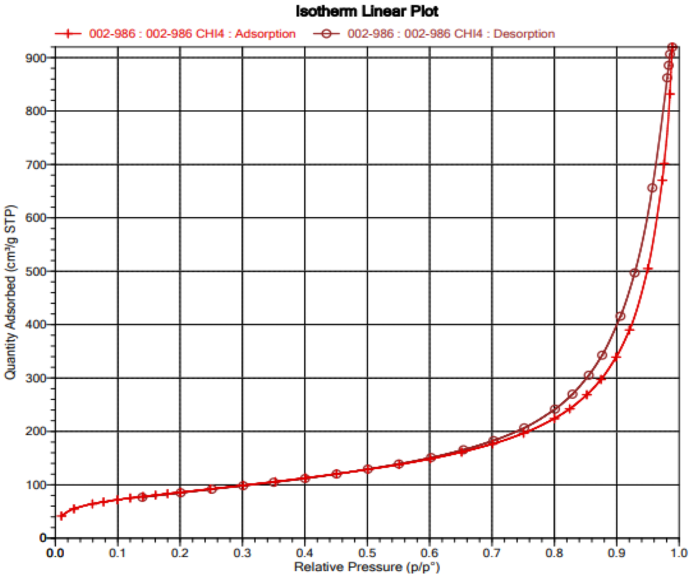

Figure 41 N$_2$ adsorption/desorption isotherm at 77 K of samples **CHT$_{2.5\%}$:EGD$_{32\%}$.**

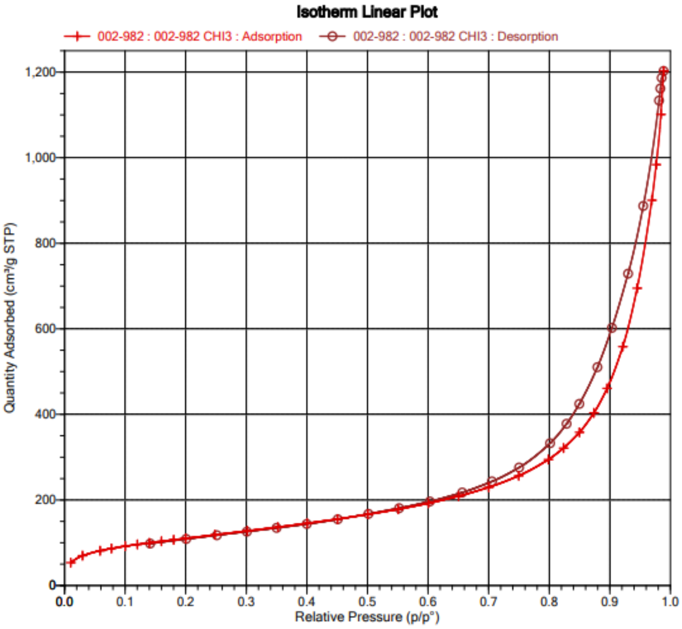

Figure 44 N$_2$ adsorption/desorption isotherm at 77 K of samples **CHT$_{2.5\%}$:EGD$_{32\%}$:IL1$_{50\%}$.**

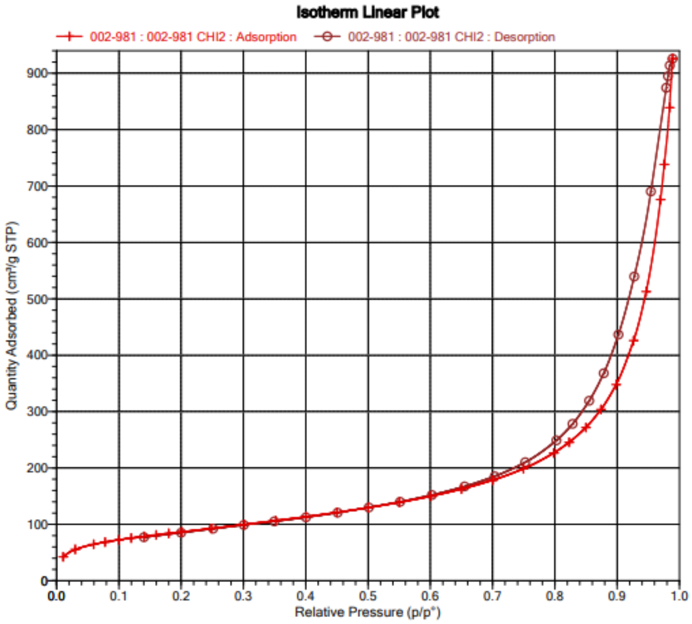

Figure 43 N$_2$ adsorption/desorption isotherm at 77 K of samples **CHT$_{2.5\%}$:EGD$_{32\%}$:IL1$_{30\%}$.**

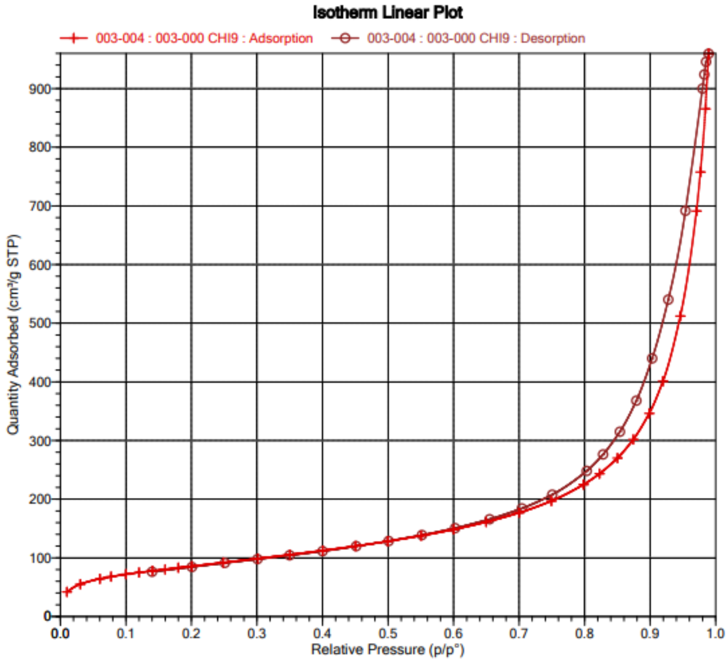

Figure 48 N_2 adsorption/desorption isotherm at 77 K of samples **CHT$_{2.5\%}$:PIL$_{15\%}$.**

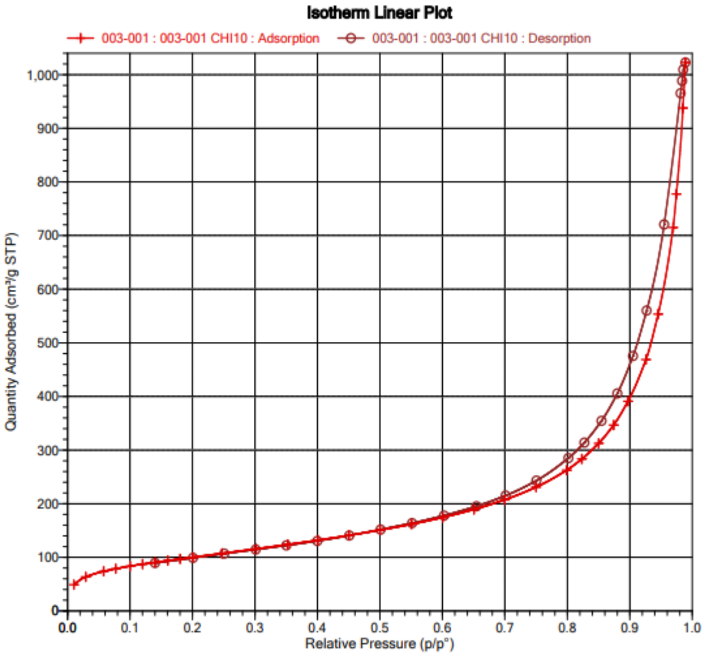

Figure 47 N_2 adsorption/desorption isotherm at 77 K of samples **CHT$_{2.5\%}$:EGD$_{32\%}$:PIL$_{7.5\%}$.**

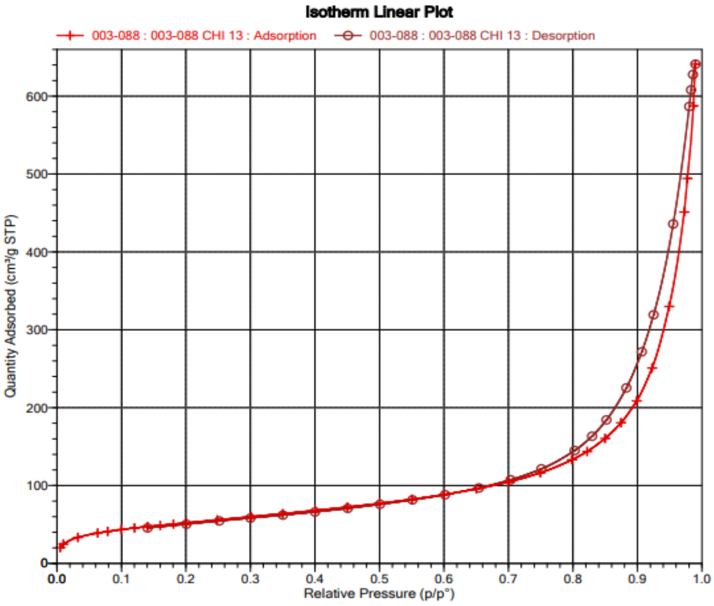

Figure 45 N_2 adsorption/desorption isotherm at 77 K of samples **CHT$_{2.5\%}$:STR$_{10\%}$:EGD$_{32\%}$:IL1$_{50\%}$.**

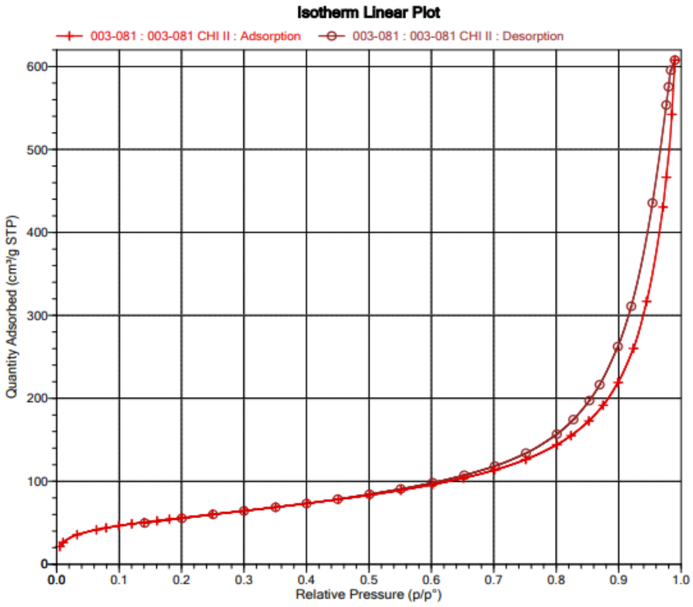

Figure 46 N_2 adsorption/desorption isotherm at 77 K of samples **CHT$_{1.5\%}$:EGD$_{32\%}$:PIL$_{50\%}$.**

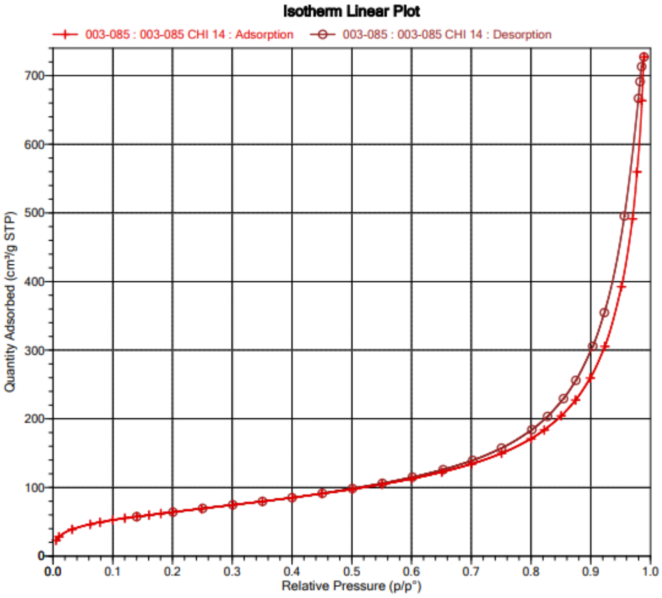

Figure 49 **CHT$_{2.5\%}$:STR$_{10\%}$:EGD$_{32\%}$:PIL$_{50\%}$.**

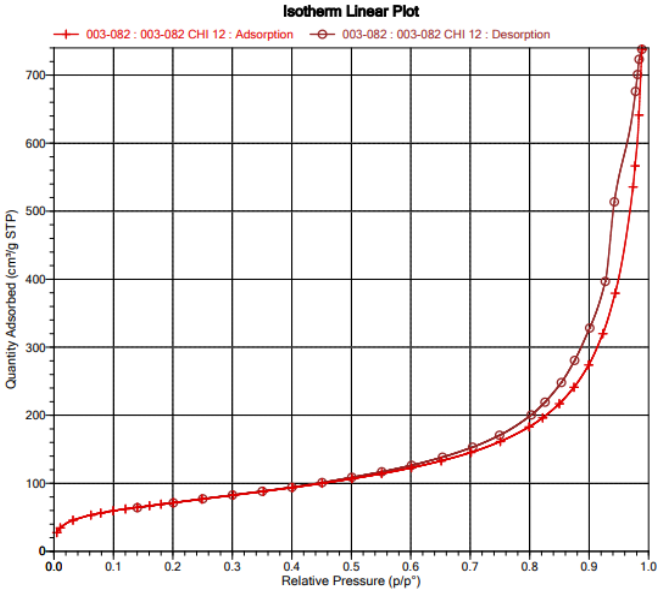

Figure 50 **CHT$_{2.0\%}$:EGD$_{32\%}$:PIL$_{50\%}$.**

A.5 Catalytic activity of *AEROSAILs*

The conversion of the reaction in batch was determined by calculating the moles of epoxide, diol, and cyclic carbonate, derived from the integration of the respective signals in the ^{1}H NMR spectra.

$$\text{Conversion\%} = \frac{[mol\ of\ reaction\ products]}{[mol\ of\ reaction\ produts + mol\ of\ unreacted\ epoxide]} \times 100$$

$$\text{Selectivity\%} = \frac{[mol\ of\ cyclic\ carbonate]}{[mol\ of\ reaction\ products]} \times 100$$

$$mol\ of\ reaction\ products = mol\ of\ cyclic\ carbonate + mol\ of\ diol\ (if\ present)$$

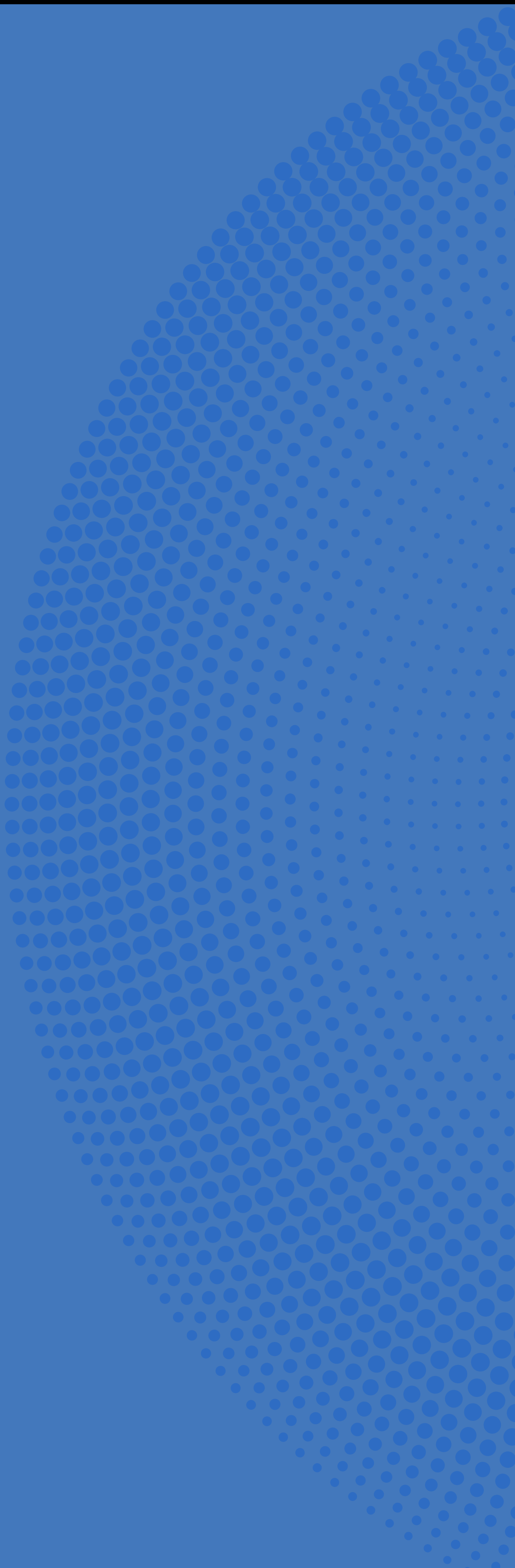

2024

Guilherme Dinis Dias Valente

DESIGNING SURFACTANT IONIC LIQUID-BASED COMPOSITES FOR CO_2 CAPTURE AND CONVERSION

NOVA SCHOOL OF
SCIENCE & TECHNOLOGY